Coverage and Throughput Analysis for Peer-to-Peer 6G Directional Slotted Aloha Bursty Networks

Massimiliano Comisso, *Member, IEEE*, Francesca Vatta, *Member, IEEE*, Giulia Buttazzoni, *Member, IEEE*, and Fulvio Babich, *Senior Member, IEEE*

***Abstract*—This paper presents a theoretical framework for investigating the coverage and throughput behavior of sixth generation (6G) peer-to-peer (P2P) directional slotted Aloha (DirSA) networks managing bursty traffic flows. Proper channel models, accounting for interference, noise, path-loss, random node location, power fluctuation, and beam pointing error, are adopted to derive analytical expressions for the statistic of the received power in ground, air, and space propagation contexts. The resulting coverage probability, obtained in simple integral form for different omnidirectional/directional transmission/reception modes, is exploited to derive multidimensional Markov chains for estimating the throughput in the absence and in the presence of a feedback mechanism, considering also the impact of the initial access procedure and of the beam training overhead. The theoretical results, which are validated by exhaustive Monte Carlo simulations, are used to evaluate the influence of the code-modulation scheme, of the operating signal to interference plus noise ratio (SINR), and of the burst length on the performance of 6G terrestrial, aerial, and satellite P2P DirSA subnets.**

***Index Terms*—Peer-to-peer (P2P), 6G, directional slotted Aloha (DirSA), coverage probability, throughput analysis.**

I. Introduction

THE challenging design of the sixth-generation (6G) ecosystem has to deal with impressive research issues, not simply limited to the embedding of the fifth-generation (5G) advanced features in the novel global standard, but also to their full deployment and overcoming. The provisioning of further evolved services, such as holoportation and virtual haptic communication, is in fact ubiquitously requested to cover land, air, and space contexts [1]. As a consequence, the possible presence of ground micro-robot swarms [2], nano-unmanned aerial vehicle (UAV) fleets [3], and low-Earth orbit (LEO) pico-satellite lattices [4], might become actually familiar for the exchange of irregular traffic flows. Within these subnets, the implementation of Internet of Things (IoT) functionalities, massive multiple input multiple output (mMIMO) technology, and device-to-device (D2D) connectivity [5], portends, for the by now near future, an extensive use of directional peer-to-peer (P2P) networking for offloading and local processing purposes on a random access basis [6]. The investigation of the actual benefits obtainable by this architecture in different 6G microwave (μWave) and millimeter-wave (mmWave) propagation contexts is still in progress, but can already rely on some valuable contributions.

Manuscript received 8 February 2023; revised 13 September 2023; accepted 26 October 2023. Date of publication 3 November 2023; date of current version 14 March 2024. This work was supported by the Italian Ministry of University and Research (MIUR) within the project FRA 2023 (University of Trieste, Italy) under Grant D13-FRA-23-Line A. The review of this article was coordinated by Dr. Cailian Chen. *(Corresponding author: Massimiliano Comisso.)*

The author are with the Department of Engineering and Architecture (DIA), University of Trieste, 34127 Trieste, Italy, and also with the National Inter-University Consortium for Telecommunications (CNIT), 50139 Florence, Italy (e-mail: mcomisso@units.it; vatta@units.it; gbuttazzoni@units.it; babich@units.it).

Digital Object Identifier 10.1109/TVT.2023.3328781

A. Related Work

From the physical (PHY) and medium access control (MAC) layers perspective, the recent research efforts on distributed P2P networks exploiting directional antennas have explored two main issues: the design of novel random access mechanisms [7], [8], [9], [10], [11], and the development of theoretical models able to reliably identify the achievable performance [12], [13], [14], [15], [16], [17], [18], [19], [20]. Since the here proposed work focuses on this latter aspect, lets briefly outline the second set of studies.

The behavior of a P2P directional slotted Aloha (DirSA) network is carefully investigated in [12], by studying the impact of the code-modulation scheme and of the beam pointing error on the node throughput, under the assumptions of pre-aligned beams. Suitable scaling laws for the sum rate of a bi-directional P2P network are derived in [13], by evaluating the asymptotic probability density function (pdf) of the signal to interference ratio (SIR) in the presence of MIMO systems not relying on instantaneous channel state information. An interesting interference analysis for P2P DirSA networks with pre-aligned antenna patterns and fixed source-destination distances is developed in [14], by discussing the adoption of a pseudowired model for highly directional mmWave links in not too dense scenarios. This issue is deepened in [15], where, still assuming pre-aligned beams, the applicability of the transition from an interference-limited to a noise-limited regime is revisited for different access schemes and obstacle densities. A DirSA scenario with pre-aligned beams is considered in [16], to estimate the cumulative distribution function (cdf) of the signal to interference plus noise ratio (SINR) in ad hoc networks supporting D2D connections, with the final aim of evaluating the benefits of directionality on the area spectral efficiency. An accurate PHY layer analysis for ad hoc directional mmWave networks is developed in [17], where closed-form expressions for the coverage probability are provided to prove its increase as a non-decreasing concave

function of the antenna array size. A further PHY layer model for distributed directional P2P networks is presented in [18], where the coverage probability is exploited to show that the interference approximation determines the antenna pattern requirements necessary to match the noise-limited assumption. A mixed aerial/terrestrial IoT P2P scenario is addressed in [19], by deriving the ergodic rate in the presence of ground transmitters with steerable dipole antennas and UAV receivers with omnidirectional radiators. A P2P DirSA scheme including the initial access procedure is explored in [20], but assuming omnidirectional transmissions and a Rayleigh fading channel.

B. Motivation and Contribution

With reference to this overview, one may notice that, in [13], [17], [18], [19], the developed analyses, although really accurate, do not incorporate the random access evolution, while, in [12], [14], [15], [16], this latter element is properly investigated, but considering pre-aligned beams. A preliminary work including the initial access stage, which has been deeply explored in [21], [22], has been carried out in [20], but adopting a partial directionality and an oversimplified channel statistic. Besides, the frameworks derived in [14], [16], [17] employ the dipole assumption, in which the source-destination distance is fixed and identical for all pairs. A comprehensive view of these aspects hence suggests that the availability of a MAC/PHY mathematical model for P2P DirSA networks including initial access, random source-destination distances, and realistic 6G propagation models may represent an interesting improvement.

For this reason, this paper proposes a theoretical analysis for investigating the coverage and throughput performance of 6G P2P DirSA networks with bursty traffic and random source-destination distances. Suitable ground, air, and space propagation models, including spatial statistic, noise, interference, path-loss attenuation, random power variation, and antenna pointing error, are used to estimate the coverage probability for different omnidirectional/directional antenna operation modes. This latter quantity, which is expressed in simple integral form, is employed to develop appropriate multidimensional Markov chains for calculating the DirSA throughput, considering two options for initial access procedure: a first one not providing a feedback mechanism, called DirSA no feedback (DirSA-NF), and a second one instead providing it, called DirSA feedback (DirSA-F). The analytical results, whose accuracy is numerically checked through exhaustive simulations, are exploited to discuss the influence of the burst length, of the operating SINR, and of the code-modulation pair on the DirSA performance for vehicle, drone, and satellite P2P networks.

The paper is organized as follows. Section II introduces the scenario. Sections III and IV present the coverage and throughput analyses, respectively. Section V discusses the numerical results. Finally, Section VI summarizes the conclusions.

Notation: Throughout the paper the following notation is used: $\mathbb{N}/\mathbb{N}_0$ denote natural numbers with/without zero; $\mathbb{R}_{>0}/\mathbb{R}_{\geq 0}$ denote positive/non-negative reals; $(\cdot)^+$ denotes positive part; $\langle \cdot, \cdot \rangle$ denotes scalar product; $||\cdot||_1$ denotes Manhattan norm; $\delta_{tt'}$ denotes Kronecker delta; $\mathbb{1}_{\mathbf{X}}(x)$ denotes indicator function; $\delta(x)$ denotes delta function; $\mathrm{erf}(x)$ denotes error function; $\Gamma(x)$ denotes gamma function; $\gamma(\cdot; x)$ denotes lower incomplete gamma function; $\mathbb{E}_X[f(X)]$ denotes expectation of function $f(X)$ over random variable (rv) X; and

$$\mathcal{B}_{t'}^{t}(x) = \binom{t}{t'} x^{t'}(1-x)^{t-t'}, \quad t, t' \in \mathbb{N};\ t' \leq t, \tag{1}$$

denotes binomial function. Basic symbols representing physical quantities are listed in Table I.

II. System Model

The description of the addressed scenario is subdivided into three parts: the arrival process and the random access mechanism are introduced in the next subsection, the antenna and code-modulation models are exposed in Section II-B, while the propagation channels for the terrestrial, aerial, and spatial environments are presented in Section II-C.

A. Access Layer

Consider a frameless P2P SA network with an infinite number of identical source-destination pairs (infinite population model) [23], and a reference space consisting of a ball of radius $\rho\,(>0)$ and dimension $\nu \in \{2, 3\}$. For each pair, the arrival event consists of a burst of b consecutive packets, where the b value is the realization of a geometric rv B having probability mass function (pmf) [24]:

$$f_B(b; \bar{b}) = \frac{1}{\bar{b}} \left(1 - \frac{1}{\bar{b}}\right)^{b-1}, \quad b \in \mathbb{N}_0, \tag{2}$$

in which $\bar{b}$ denotes the average burst length. According to the typical SA settings, the transmission time τ of a packet is in general assumed equal to the slot duration, while retransmissions are not allowed, thus, once transmitted, any packet is discarded from the queue of the source regardless of the result of the reception attempt. Besides, the number i of bursts generated in the network for a given offered load $\varsigma\ (\geq 0)$ is the realization of a Poisson rv I with pmf [24]:

$$f_I(i; \varsigma) = \frac{\varsigma^i}{i!} \exp(-\varsigma), \quad i \in \mathbb{N}. \tag{3}$$

This realization i also describes the number of pairs activated inside the population. The reciprocal interference between these pairs can be managed by exploiting the beamforming capabilities of the nodes, since they are assumed equipped with analog antenna systems enabling the synthesis of directional transmitting and/or receiving patterns. This leads to a DirSA scheme, in which, with reference to a burst arrived at a target source S and intended for a target destination D, the transmission/reception process may be subdivided in two stages: the initial access (IA) and the subsequent block acquisition (BA). The evolution of these stages depends on the absence or presence of a feedback response sent by D to S within the IA stage. Lets hence separately consider these two options, which are respectively identified as DirSA-NF and DirSA-F.

1) DirSA-NF: Adopting this option, the transmission/reception process started at a generic slot s evolves according to Fig. 1(a). During the IA stage, S omnidirectionally transmits (oT mode) the first packet P_1 of the burst that

TABLE I
BASIC SYMBOLS

B	Burst length (rv)
$\bar{b}$	Average burst length
D	Target destination
$\mathcal{E}_\epsilon(\cdot)$	Training efficiency for DirSA option ϵ
$\mathcal{F}_\mathrm{R}$	Receiver noise figure
$\bar{G}$	Maximum antenna gain
$\bar{g}$	Backlobe antenna gain
$G_{\mathrm{T}_l}^{h_\mathrm{T}}/G_{\mathrm{R}_l}^{h_\mathrm{R}}$	Transmitting/receiving antenna gain in mode $h_\mathrm{T}/h_\mathrm{R}$ referred to transmitter l (rv)
$G_l^{h_\mathrm{T}h_\mathrm{R}}$	Antenna product gain in mode $(h_\mathrm{T},h_\mathrm{R})$ referred to transmitter l (rv)
$h_\mathrm{T}/h_\mathrm{R}$	Antenna transmission/reception mode 0: omnidirectional, 1: directional
I	Number of generated bursts (rv)
$\mathcal{L}(\cdot)$	Path-loss function
m	Code-modulation model - 0: Shannon, 1: LDPC/QPSK
$\mathcal{N}$	Noise power
n	Number of transmitters
$\mathcal{O}_\epsilon(\cdot)$	Burst overhead for DirSA option ϵ
P_T	Transmission power
$P_l^{h_\mathrm{T}h_\mathrm{R}}$	Power received from transmitter l in mode $(h_\mathrm{T},h_\mathrm{R})$ (rv)
R_l	Distance from transmitter l (rv)
S	Target source
S	Network throughput
$\mathbf{s}$	Network state in a slot
T_R	Receiver temperature
$T_{\mathbf{s}'\mathbf{s}}^\epsilon(\cdot,\cdot)$	Transition probability from previous state $\mathbf{s}'$ to present state $\mathbf{s}$ for DirSA option ϵ
W_R	Receiver bandwidth
α_1/α_2	Path-loss floating intercept/exponent
ϵ	DirSA option - 1: NF, 2: F
$\eta_n^{h_\mathrm{T}h_\mathrm{R}}(\cdot)$	Coverage probability for n transmitters in mode $(h_\mathrm{T},h_\mathrm{R})$
$\eta_\mathbf{s}^\epsilon(\cdot)$	Joint coverage probability in state $\mathbf{s}$ for DirSA option ϵ
$\tilde{\eta}_i^{\mathrm{IA}}(\cdot)/\hat{\eta}_i^{\mathrm{IA}}(\cdot)$	Coverage probability for DirSA-NF/F with i sources at initial access stage
$\tilde{\eta}_o^{\mathrm{BA-u}}(\cdot)$	Coverage probability for DirSA-NF with o sources at block acquisition stage after unsuccessful initial access
$\tilde{\eta}_d^{\mathrm{BA-s}}(\cdot)$	Coverage probability for DirSA-NF with d sources at block acquisition stage after successful initial access
$\hat{\eta}_d^{\mathrm{BA}}(\cdot)$	Coverage probability for DirSA-F with d sources at block acquisition stage
λ	Poisson process intensity
μ_1	Nakagami parameter
μ_2/μ_3	Generalized gamma shape/scale parameters
ν	Space dimension
ρ	Cell radius
$\varrho_m(\cdot)$	Rate for code-modulation scheme m
τ	Packet transmission time, i.e., slot time
τ_H	Header transmission time
$\tilde{\sigma}$	Shadowing standard deviation
$\hat{\sigma}^2$	Antenna pointing error variance
ς	Offered load
ς_a	Actual load
υ	SINR receiving threshold
$\Upsilon_n^{h_\mathrm{T}h_\mathrm{R}}$	SINR for n transmitters in mode $(h_\mathrm{T},h_\mathrm{R})$ (rv)
$\varphi_\mathbf{s}^\epsilon(\cdot,\cdot)$	Steady-state probability in state $\mathbf{s}$ for DirSA option ϵ
Ψ_l	Power fluctuation for transmitter l (rv)
Ω	Antenna main lobe beamwidth
ω_l	Probability that transmitter l lies in antenna main lobe

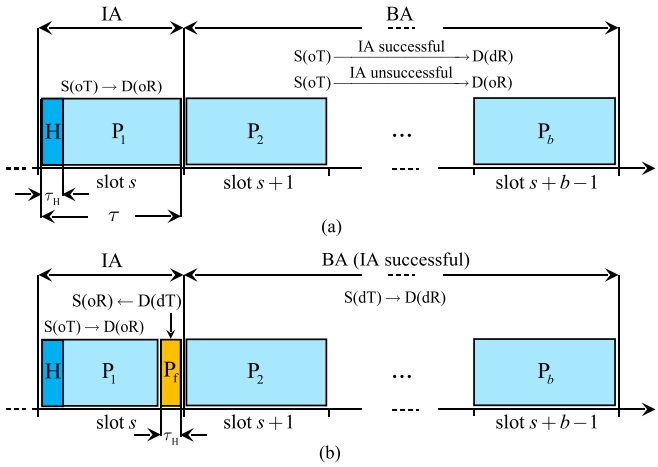

Fig. 1. Burst transmission/reception process: (a) DirSA-NF, (b) DirSA-F.

is omnidirectionally received (oR mode) by D. This first packet contains a specific header field H, characterized by a transmission time $\tau_\mathrm{H}(<\tau)$, which provides to D itself the information necessary to generate a directional pattern with the main lobe steered towards S. If this first stage is successful, the remaining $b-1$ packets $\mathrm{P}_2,\ldots,\mathrm{P}_b$ of the burst are sent in oT mode by S and directionally received (dR mode) by D. If, instead, the IA stage is unsuccessful, the same packets are still sent in oT mode by S, but they are acquired in oR mode by D. Therefore, during the BA stage, the packets $\mathrm{P}_2,\ldots,\mathrm{P}_b$ are anyway sent in oT mode, since S has no information from D to be aware of the result of the IA stage and/or to generate a directional transmitting pattern. In this case, the success or not of the IA stage just determines the selection at D of the dR mode or of the oR one for the acquisition of the rest of the burst.

2) DirSA-F: This second option evolves in agreement with Fig. 1(b), which shows that the IA stage still covers just one slot, but now involves two packets. The first one is again P_1, which, similarly to the previous option, is sent in oT mode by S, acquired in oR mode by D, and, through the header H, used to synthesize a directional pattern pointing towards S. Differently from the DirSA-NF option, P_1 is now slightly smaller and hence characterized by a transmission time $\tau-\tau_\mathrm{H}$, in order to allow D to transmit the feedback packet P_f, having the same transmission time τ_H of the header field H. This latter packet, which is directionally transmitted (dT mode) by D and acquired in oR mode by S, provides to S itself the information necessary to synthesize a directional pattern pointing towards D. If both the P_1 and P_f acquisitions are successful, the IA stage is completed and the transmission/reception process can move to the BA stage, during which the remaining $b-1$ packets of the burst are sent in dT mode by S and acquired in dR mode by D. If, instead, at least one of the two acquisitions of the IA stage is unsuccessful, the BA stage is aborted and the rest of the burst is not transmitted. In particular, this may happen because of an unsuccessful acquisition of P_1 by D, which stops the sending of P_f, or because of an unsuccessful acquisition of P_f itself by S. In all cases, S is aware of the result of the IA stage and hence has sufficient information to decide whether to transmit the rest of the burst or not.

For both options, the transmission/reception process covers b slots, and no other features, such as retransmission [8], carrier sensing [9], bi-directionality [13], interference cancellation (IC) [25], or packet repetition/coding [26], [27], are added, in order to focus on the DirSA basic functionalities in Poisson bursty traffic conditions. Besides, the IA stage always begins in oT mode to limit the access delay and the burst overhead due to the beamforming training sequence [21]. This overhead may be expressed as the ratio:

$$\mathcal{O}_{\epsilon}(b) = \frac{\epsilon\,\tau_{\mathrm{H}}}{b\,\tau}, \tag{4}$$

where:

$$\epsilon = \begin{cases} 1 & \text{DirSA-NF} \\ 2 & \text{DirSA-F} \end{cases}. \tag{5}$$

B. Physical Layer

The just outlined access rules show that, in general, the target nodes S and D might exchange their role of transmitter and receiver, while, because of the contention-based SA scenario, further transmitters, belonging to other communicating pairs, can interfere with the S or D reception. These aspects have to be considered remembering that there are four possible types of communication for the exchange of a packet. By introducing two suitable indexes h_{T} and h_{R} to describe each mode, these types may be compactly described as: oT-oR ($h_{\mathrm{T}}=h_{\mathrm{R}}=0$), oT-dR ($h_{\mathrm{T}}=0, h_{\mathrm{R}}=1$), dT-oR ($h_{\mathrm{T}}=1, h_{\mathrm{R}}=0$), dT-dR ($h_{\mathrm{T}}=h_{\mathrm{R}}=1$). Therefore, when $n\in\mathbb{N}_0$ simultaneously active nodes (one target transmitter and $n-1$ interferers) operate in mode h_{T}, the power incoming from the generic l-th transmitter to the target receiver operating in mode h_{R} may be expressed, for $l=1,\ldots,n$ and $h_{\mathrm{T}}, h_{\mathrm{R}}=0, 1$, by defining the rv:

$$P_l^{h_{\mathrm{T}}h_{\mathrm{R}}} = P_{\mathrm{T}} G_{\mathrm{T}_l}^{h_{\mathrm{T}}} G_{\mathrm{R}_l}^{h_{\mathrm{R}}} \mathcal{L}(R_l)\Psi_l, \tag{6}$$

where $P_{\mathrm{T}}(\geq 0)$ is a constant representing the transmission power (assumed equal for all nodes) [15]; $G_{\mathrm{T}_l}^{h_{\mathrm{T}}}$ is a rv denoting the transmitting antenna gain of the l-th transmitter operating in mode h_{T} towards the target receiver; $G_{\mathrm{R}_l}^{h_{\mathrm{R}}}$ is a rv identifying the receiving antenna gain of the target receiver operating in mode h_{R} towards the l-th transmitter; $\mathcal{L}(R_l)$ models the path-loss as a function of the rv R_l, representing the distance between the l-th transmitter and the target receiver; while Ψ_l is a further rv modeling the statistical fluctuations (shadowing, fading, scintillation,...), which characterize the propagation channel between the l-th transmitter and the target receiver. Without loss of generality the value $l=1$ is adopted to identify the target (desired) transmitter and the values $l=2,\ldots,n$ to describe the interferers. The choice of considering also R_1 as a rv enables to model the general scenario of random source-destination distance, in which the $\mathrm{S}-\mathrm{D}$ distance itself, similarly to the interfering $R_2,\ldots,R_n$ ones, depends on the spatial statistic, thus S and D can be far or close from each other depending on the specific realization.

The antenna gain is selected equal to unity for the omnidirectional cases, while, for the directional ones, it is chosen equal to the maximum gain $\bar{G}(\geq 1)$ within the main lobe and equal to the backlobe gain $\bar{g}(\leq 1)$ outside [15]. Moreover, to account for possible antenna pointing inaccuracies, the beamsteering error is modeled by a zero-mean $\hat{\sigma}^2$-variance Gaussian pdf [28]. All these elements may be jointly taken into account by defining, for $\mathrm{N}\in\{\mathrm{T},\mathrm{R}\}$, $l=1,\ldots,n$, and $h=h_{\mathrm{T}}, h_{\mathrm{R}}\in\{0,1\}$, the pdf:

$$f_{G_{\mathrm{N}_l}^h}(g) = \begin{cases} \delta(g-1) & h=0 \\ \omega_l\,\delta(g-\bar{G}) + (1-\omega_l)\,\delta(g-\bar{g}) & h=1 \end{cases}, \tag{7}$$

where, for $h=0$, the degenerate distribution is used to include the deterministic unity gain, and [28]:

$$\omega_l = \begin{cases} \mathrm{erf}\left[\Omega/(2\sqrt{2}\hat{\sigma})\right] & l=1 \\ \Omega/[2(\nu-1)\pi] & l=2,\ldots,n \end{cases}, \tag{8}$$

in which Ω ($0\leq\Omega\leq 2(\nu-1)\pi$) is the main lobe beamwidth (measured in radians for $\nu=2$ and in steradians for $\nu=3$).

Beside the antenna system, the PHY layer accounts for the code-modulation scheme, whose usability requires that the SINR experienced at D be larger or equal to a corresponding threshold $\upsilon\in\mathbb{R}_{>0}$ [17]. This scheme is modeled considering two cases, each identified by an index m. The first one ($m=0$) is more ideal and relies on the Shannon bound, while the second one ($m=1$) is more practical and relies on a fixed quadrature phase-shift keying (QPSK) modulation combined with an efficient code, such as a turbo or a low-density parity-check (LDPC) one. For each of the two cases, the rate, representing the number of information bits carried by each transmission, symbol, or channel use, can be evaluated as [18]:

$$\varrho_m(\upsilon) = \begin{cases} \log_2(1+\upsilon) & m=0 \\ 2\min\left\{\left[1-\exp\left(\zeta_3 - \dfrac{\zeta_1\upsilon^{\zeta_2}}{2^{\zeta_2}}\right)\right]^+, 1\right\} & m=1 \end{cases}, \tag{9}$$

where $\zeta_1\cong 1.2860$, $\zeta_2\cong 0.9308$, and $\zeta_3\cong 0.0102$. As outlined in [18], the approximation for the second case in (9) guarantees an error lower than 1% with respect to the actual performance of an LDPC code for υ values not too close to zero.

C. Channel Models

The 6G ecosystem is explicitly conceived to include terrestrial, aerial, and spatial networks, thus, in such a manifold scenario, the behavior of the P2P DirSA options have to be tested considering propagation models adherent to each of the three contexts. Some elements of these models, such as the path-loss attenuation and the noise power, may be characterized by common formulas, while others, such as the spatial distribution of the nodes and the statistic of the power fluctuations, require more specific descriptions. In particular, the floating-intercept model may be in general adopted to formalize the dependence of the attenuation from the distance R_l ($l=1,\ldots,n$), thus allowing to select, for the path-loss function in (6), the expression [29]:

$$\mathcal{L}(R_l) = \frac{1}{\alpha_1 R_l^{\alpha_2}}, \tag{10}$$

where $\alpha_1(\geq 1)$ denotes the floating intercept and $\alpha_2(\geq 2)$ represents the average path-loss exponent. Another quantity common to the three contexts is the noise power, which can be evaluated

at a receiver as [28]:

$$\mathcal{N} = \kappa_{\mathrm{B}} T_{\mathrm{R}} W_{\mathrm{R}} \mathcal{F}_{\mathrm{R}}, \tag{11}$$

where $\kappa_{\mathrm{B}} \cong 1.38 \cdot 10^{-23}$ J/K is the Boltzmann constant, while T_{R}, W_{R}, and $\mathcal{F}_{\mathrm{R}}$ are the temperature, bandwidth, and noise figure of the receiver, respectively. The specific values of these parameters and of the path-loss ones are of course dependent on the specific context (ground, air, or space). Just the context determines the statistics of the two other rvs R_l and Ψ_l in (6), whose description requires dedicated formulations.

1) Terrestrial Environment: The most widely adopted spatial statistic for ground-based networks is the two-dimensional (2D) homogeneous Poisson point process (HPPP) [16], which has the advantage of often providing mathematically tractable frameworks thanks to the independence property. Remembering that, for $\nu = 2$, the cell identifying the reference space is a disk of radius ρ, the intensity of the HPPP on $\mathbb{R}^2$ for n active pairs results equal to $n/(\pi\rho^2)$. By recalling the thinning property, this original process may be partitioned into n independent HPPPs, each characterized by an intensity:

$$\lambda = \frac{1}{\pi\rho^2}, \tag{12}$$

for which the cdf of the distance R_l for $l = 1, \ldots, n$ may be expressed as [28]:

$$F_{R_l}(r) = \left[1 - \exp\left(-\pi\lambda r^2\right)\right] \mathbb{1}_{\mathbb{R}_{\geq 0}}(r). \tag{13}$$

In the mmWave terrestrial environment, the main statistical phenomenon determining power fluctuations is shadowing, since the very low carrier wavelengths adopted for the transmission of the signals are really sensitive to both large and small obstacles at the ground level. This phenomenon may be modeled through a log-normal distribution, whose pdf, referred to the rv Ψ_l for $l = 1, \ldots, n$, may be written as [29]:

$$f_{\Psi_l}(\psi) = \frac{1}{\sqrt{2\pi}\tilde{\sigma}\psi} \exp\left(-\frac{\log^2 \psi}{2\tilde{\sigma}^2}\right) \mathbb{1}_{\mathbb{R}_{>0}}(\psi), \tag{14}$$

where $\tilde{\sigma}$ is the shadowing standard deviation.

2) Aerial Environment: The stochastic modeling of UAV networks has to account for the random location of devices flying in dynamic formation within the reference space identifying the cell, in this case represented by a ball of radius ρ and dimension $\nu = 3$. This context may be suitably described by a three-dimensional (3D) random waypoint mobility model (RWMM) [30], in which the target node uniformly chooses a speed inside a limited interval and a position inside the cell, then moving in the selected direction. When the position is reached, the node awaits a certain time, subsequently choosing a further speed and a further position. The iteration of this procedure for many times, thus approaching infinity, leads to a speed-independent asymptotic distribution for the distance R_l, whose cdf may be expressed, for $l = 1, \ldots, n$, as [18]:

$$F_{R_l}(r) = \left[\sum_{k=1}^{3} a_k \left(\frac{r}{\rho}\right)^{2k+1}\right] \mathbb{1}_{[0,\rho]}(r) + \mathbb{1}_{]\rho,+\infty[}(r), \tag{15}$$

where $a_1 = 245/72$, $a_2 = -119/36$, and $a_3 = 65/72$. Differently from the terrestrial case, the reasonable absence of obstacles among the flying UAVs and their high degree of mobility make small-scale fading more relevant than shadowing for the power fluctuations. By consequence, adopting a Nakagami fading model, the rv Ψ_l, for $l = 1, \ldots, n$, can be described through a gamma distribution, having pdf [30]:

$$f_{\Psi_l}(\psi) = \frac{\mu_1^{\mu_1}}{\Gamma(\mu_1)} \psi^{\mu_1 - 1} \exp\left(-\mu_1 \psi\right) \mathbb{1}_{\mathbb{R}_{\geq 0}}(\psi), \tag{16}$$

where $\mu_1 (\geq 1/2)$ denotes the shape (or Nakagami) parameter.

3) Spatial Environment: The distributed P2P architecture is becoming of interest also for the space context, since the recent developments in spatial communications consider the launch from a LEO mothership of swarms of very small satellites (CubeSats, PocketQubes, or SunCubes) for Earth observation applications [4]. The moving of these swarms in planar formations makes suitable the adoption, for the stochastic spacecraft location, of a uniform distribution (UD) over a reference space of dimension $\nu = 2$, consisting of a disk of radius ρ. Accordingly, the cdf of the distance R_l for $l = 1, \ldots, n$, may be written as [4]:

$$F_{R_l}(r) = \left(\frac{r}{\rho}\right)^2 \mathbb{1}_{[0,\rho]}(r) + \mathbb{1}_{]\rho,+\infty[}(r). \tag{17}$$

The regular reciprocal positions of the small satellites within the swarm and the free space propagation conditions suggest a negligible impact of the obstacles and of the relative mobility on the received signals. Random power variations are in this case due to scintillation, a fluctuation determined by irregularities in the free-electron concentration of the ionosphere. One of the most versatile statistics for describing this activity is the generalized gamma distribution, whose pdf, referred to the rv Ψ_l, for $l = 1, \ldots, n$, may be expressed as [31]:

$$f_{\Psi_l}(\psi) = \frac{\mu_2 \psi^{\mu_1\mu_2 - 1}}{\mu_3^{\mu_1\mu_2}\Gamma(\mu_1)} \exp\left[-\left(\frac{\psi}{\mu_3}\right)^{\mu_2}\right] \mathbb{1}_{\mathbb{R}_{\geq 0}}(\psi), \tag{18}$$

where μ_1 and μ_2 are shape parameters, while:

$$\mu_3 = \frac{\Gamma(\mu_1)}{\Gamma\left(\mu_1 + \dfrac{1}{\mu_2}\right)}, \tag{19}$$

is a scale parameter. As expected, by selecting $\mu_2 = 1$ in (18) and (19), one obtains $\mu_3 = 1/\mu_1$ and then (16).

III. Coverage Analysis

The illustrated system model is used to estimate the coverage probability referred to the single packet for the different transmission/reception modes and propagation contexts, with the aim of subsequently evaluating the network throughput for the analyzed P2P DirSA-NF and DirSA-F schemes in the presence of burst traffic. The first task is performed in this section, while the second one is addressed in Section IV.

Lets start the coverage analysis by preliminarily considering the product gain:

$$G_l^{h_{\mathrm{T}} h_{\mathrm{R}}} = G_{\mathrm{T}_l}^{h_{\mathrm{T}}} G_{\mathrm{R}_l}^{h_{\mathrm{R}}}, \tag{20}$$

which statistically models the effect of the reciprocal orientation of the antennas on the received power. The pdf of this rv can be calculated through the following lemma.

Lemma 1 (Product gain pdf): Let $G_{\mathrm{T}_l}^{h_{\mathrm{T}}}$ and $G_{\mathrm{R}_l}^{h_{\mathrm{R}}}$ be distributed according to (7). Then, for $l=1,\ldots,n$ and $h_{\mathrm{T}},h_{\mathrm{R}}\in\{0,1\}$, the pdf of $G_l^{h_{\mathrm{T}}h_{\mathrm{R}}}$ can be evaluated by (21) shown at the bottom of this page, in which:

$$\varepsilon_{ljj'}=\omega_l^2\left(\frac{1}{\omega_l}-1\right)^{j+j'}, \tag{22a}$$

$$\chi_{jj'}=\bar{G}^2\left(\frac{\bar{g}}{\bar{G}}\right)^{j+j'}. \tag{22b}$$

Proof: See Appendix A. □

Using this result and substituting (10) into (6), the received power can be expressed, for $l=1,\ldots,n$ and $h_{\mathrm{T}},h_{\mathrm{R}}=0,1$, as:

$$P_l^{h_{\mathrm{T}}h_{\mathrm{R}}}=Q_lG_l^{h_{\mathrm{T}}h_{\mathrm{R}}}, \tag{23}$$

where:

$$Q_l=\frac{\theta\Psi_l}{R_l^{\alpha_2}}, \tag{24}$$

with $\theta=P_{\mathrm{T}}/\alpha_1$. This reformulation enables to gather the context-specific quantities in the rv Q_l, whose statistic can be derived by the following lemmas for the three environments.

Lemma 2 (Q_l statistics - Ground): Let R_l be distributed according to (13) and Ψ_l according to (14). Then, for $l=1,\ldots,n$, the cdf and pdf of Q_l can be respectively estimated as:

$$F_{Q_l}(q)\cong\left[\sum_{k\in\mathbb{D}^{\mathrm{t}}}A_k^{\mathrm{t}}W_k^{\mathrm{t}}(q)\right]\mathbb{1}_{\mathbb{R}_{>0}}(q), \tag{25a}$$

$$f_{Q_l}(q)\cong\frac{\beta^{\mathrm{t}}}{q^{\beta^{\mathrm{t}}+1}}\left[\sum_{k\in\mathbb{D}^{\mathrm{t}}}A_k^{\mathrm{t}}c_k^{\mathrm{t}}W_k^{\mathrm{t}}(q)\right]\mathbb{1}_{\mathbb{R}_{>0}}(q), \tag{25b}$$

where $\mathbb{D}^{\mathrm{t}}=\{-1,0,1\}$, and:

$$A_k^{\mathrm{t}}=\frac{2}{3\cdot4^{|k|}}, \tag{26a}$$

$$W_k^{\mathrm{t}}(q)=\exp\left(-\frac{c_k^{\mathrm{t}}}{q^{\beta^{\mathrm{t}}}}\right), \tag{26b}$$

$$c_k^{\mathrm{t}}=\pi\lambda\theta^{\beta^{\mathrm{t}}}\exp\left(\sqrt{3}\tilde{\sigma}\beta^{\mathrm{t}}k\right), \tag{26c}$$

$$\beta^{\mathrm{t}}=\frac{2}{\alpha_2}. \tag{26d}$$

Proof: See Appendix B. □

Lemma 3 (Q_l statistics - Air): Let R_l be distributed according to (15) and Ψ_l according to (16). Then, for $l=1,\ldots,n$, the cdf and pdf of Q_l are respectively given by:

$$F_{Q_l}(q)=\left[\sum_{k\in\mathbb{D}^{\mathrm{a}}}A_k^{\mathrm{a}}W_k^{\mathrm{a}}(q)\right]\mathbb{1}_{\mathbb{R}_{>0}}(q), \tag{27a}$$

$$f_{Q_l}(q)=\frac{1}{q}\left\{\sum_{k\in\mathbb{D}^{\mathrm{a}}}A_k^{\mathrm{a}}\left[Z_k^{\mathrm{a}}(q)-\beta_k^{\mathrm{a}}W_k^{\mathrm{a}}(q)\right]\right\}\mathbb{1}_{\mathbb{R}_{>0}}(q), \tag{27b}$$

where $\mathbb{D}^{\mathrm{a}}=\{0,1,2,3\}$, and:

$$A_k^{\mathrm{a}}=-\frac{a_k}{\Gamma(\mu_1)}\left(\frac{c^{\mathrm{a}}}{\mu_1}\right)^{\beta_k^{\mathrm{a}}}, \tag{28a}$$

$$W_k^{\mathrm{a}}(q)=\frac{1}{q^{\beta_k^{\mathrm{a}}}}\gamma\left(\mu_1+\beta_k^{\mathrm{a}};\frac{\mu_1}{c^{\mathrm{a}}}q\right), \tag{28b}$$

$$Z_k^{\mathrm{a}}(q)=\left(\frac{\mu_1}{c^{\mathrm{a}}}\right)^{\mu_1+\beta_k^{\mathrm{a}}}q^{\mu_1}\exp\left(-\frac{\mu_1}{c^{\mathrm{a}}}q\right), \tag{28c}$$

$$c^{\mathrm{a}}=\frac{\theta}{\rho^{\alpha_2}}, \tag{28d}$$

$$\beta_k^{\mathrm{a}}=(1-\delta_{0\,k})\,\frac{2k+1}{\alpha_2}, \tag{28e}$$

with $a_0=-1$.

Proof: See Appendix C. □

Lemma 4 (Q_l statistics - Space): Let R_l be distributed according to (17) and Ψ_l according to (18). Then, for $l=1,\ldots,n$, the cdf and pdf of Q_l are respectively given by:

$$F_{Q_l}(q)=\left[\sum_{k\in\mathbb{D}^{\mathrm{s}}}A_k^{\mathrm{s}}W_k^{\mathrm{s}}(q)\right]\mathbb{1}_{\mathbb{R}_{>0}}(q), \tag{29a}$$

$$f_{Q_l}(q)=\frac{1}{q}\left\{\sum_{k\in\mathbb{D}^{\mathrm{s}}}A_k^{\mathrm{s}}\left[Z_k^{\mathrm{s}}(q)-\beta_k^{\mathrm{s}}W_k^{\mathrm{s}}(q)\right]\right\}\mathbb{1}_{\mathbb{R}_{>0}}(q), \tag{29b}$$

where $\mathbb{D}^{\mathrm{s}}=\{0,1\}$, and:

$$A_k^{\mathrm{s}}=\frac{(-1)^k}{\Gamma(\mu_1)}\left(c^{\mathrm{s}}\mu_3\right)^{\beta_k^{\mathrm{s}}}, \tag{30a}$$

$$W_k^{\mathrm{s}}(q)=\frac{1}{q^{\beta_k^{\mathrm{s}}}}\gamma\left[\mu_1+\frac{\beta_k^{\mathrm{s}}}{\mu_2};\left(\frac{q}{\mu_3c^{\mathrm{s}}}\right)^{\mu_2}\right], \tag{30b}$$

$$Z_k^{\mathrm{s}}(q)=\frac{\mu_2q^{\mu_1\mu_2}}{(\mu_3c^{\mathrm{s}})^{\mu_1\mu_2+\beta_k^{\mathrm{a}}}}\exp\left[-\left(\frac{q}{\mu_3c^{\mathrm{a}}}\right)^{\mu_2}\right], \tag{30c}$$

$$c^{\mathrm{s}}=c^{\mathrm{a}}, \tag{30d}$$

$$\beta_k^{\mathrm{s}}=\frac{2\,k}{\alpha_2}. \tag{30e}$$

$$f_{G_l^{h_{\mathrm{T}}h_{\mathrm{R}}}}(g)=\begin{cases}\delta(g-1) & (h_{\mathrm{T}},h_{\mathrm{R}})=(0,0)\\ \omega_l\delta\left(g-\bar{G}\right)+(1-\omega_l)\,\delta(g-\bar{g}) & (h_{\mathrm{T}},h_{\mathrm{R}})\in\{(1,0),(0,1)\}\\ \sum_{j,j'=0}^{1}\varepsilon_{ljj'}\delta(g-\chi_{jj'}) & (h_{\mathrm{T}},h_{\mathrm{R}})=(1,1)\end{cases} \tag{21}$$

Proof: See Appendix D. □

Among the three derived statistics, those referred to the aerial and spatial contexts are exact, while that referred to the terrestrial environment is approximated, because of the impossibility of solving the involved integral in closed-form. The accuracy of the adopted approximation will be checked during the discussion of the numerical results. Now that the statistics of Q_l and of the product gain are available, the cdf and pdf of the received power in (23) can be calculated. This task can be accomplished through the following proposition.

Proposition 1 (Power statistics): Let $G_l^{h_\mathrm{T}h_\mathrm{R}}$ be distributed according to (21) and Q_l according to (25), (27), or (29) for the ground, air, and space contexts, respectively. Then, for $l=1,\ldots,n$ and $h_\mathrm{T},h_\mathrm{R}\in\{0,1\}$, the cdf and pdf of the received power may be respectively evaluated by (31a) and (31b), both shown at the bottom of this page.

Proof: See Appendix E. □

The characterization of the desired ($l=1$) and of the interfering ($l=2,\ldots,n$) powers allows one to analyze the SINR for the target $\mathrm{S}-\mathrm{D}$ communication, which may be expressed, for each $(h_\mathrm{T},h_\mathrm{R})$ type, through the rv:

$$\Upsilon_n^{h_\mathrm{T}h_\mathrm{R}}=\frac{P_1^{h_\mathrm{T}h_\mathrm{R}}}{\sum_{l=2}^{n}P_l^{h_\mathrm{T}h_\mathrm{R}}+\mathcal{N}}, \tag{32}$$

with the noise power given by (11). The success of this communication occurs when the realization of $\Upsilon_n^{h_\mathrm{T}h_\mathrm{R}}$ is larger or equal to the SINR value υ, determining the rate according to (9). Therefore, for each pair of transmission/reception modes, the complementary cdf (ccdf) of the SINR provides the coverage probability, whose calculation enables the formulation of the following proposition.

Proposition 2 (Coverage probability): Let $P_l^{h_\mathrm{T}h_\mathrm{R}}$ be distributed according to (31) and the noise power given by (11). Then, for $n\in\mathbb{N}_0$, $h_\mathrm{T},h_\mathrm{R}\in\{0,1\}$, and $\upsilon\in\mathbb{R}_{>0}$, the coverage probability may be estimated as:

$$\eta_n^{h_\mathrm{T}h_\mathrm{R}}(\upsilon)\cong\begin{cases}F_{P_1^{h_\mathrm{T}h_\mathrm{R}}}(\mathcal{N}\upsilon) & n=1\\ \displaystyle\int_{\mathcal{N}\upsilon}^{+\infty}F^{n-1}_{P^{h_\mathrm{T}h_\mathrm{R}}_{l\geq 2}}\left(\frac{p}{\upsilon}-\mathcal{N}\right)f_{P_1^{h_\mathrm{T}h_\mathrm{R}}}(p)\,\mathrm{d}p & n\geq 2\end{cases}. \tag{33}$$

Proof: See Appendix F. □

This result concludes the first part of the analysis, which in the complex requires a unique numerical integration, since, except from the final expression in (33), all the other derived quantities have been obtained in analytical form.

IV. Throughput Analysis

As a preliminary step for the throughput evaluation, lets firstly consider the presence of the beamforming training sequence (Fig. 1), whose average impact can be estimated through the following lemma.

Lemma 5 (Training efficiency): Let B be distributed according to (2) and $\mathcal{O}_\epsilon(b)$ defined by (4). Then, for $\epsilon=1,2$, the average DirSA efficiency with respect to the beamforming training sequence is given by:

$$\mathcal{E}_\epsilon(\bar{b})=1-\epsilon\,\frac{\tau_\mathrm{H}\log\bar{b}}{\tau(\bar{b}-1)}. \tag{34}$$

Proof: See Appendix G. □

Once the training efficiency and the coverage probabilities for the four types of communication are available, the throughput for the P2P DirSA-NF and DirSA-F schemes can be calculated by exploiting the Markov chain models presented in [20], which are here for completeness more deeply explained and extended to include the fully directional case. In particular, the first option is analyzed in the next subsection, while the second one is investigated in Section IV-B. In both cases, the additional coverage value $\eta_0^{h_\mathrm{T}h_\mathrm{R}}(\upsilon)=1$, for $h_\mathrm{T},h_\mathrm{R}\in\{0,1\}$ and $\upsilon\in\mathbb{R}_{>0}$, is introduced for mathematical purposes.

A. DirSA-NF

As outlined in Section II-A, when the feedback mechanism is not available, the BA stage anyway begins, but relying on an $(h_\mathrm{T},h_\mathrm{R})=(0,0)$ (oT-oR) communication type if the IA stage is unsuccessful, and on an $(h_\mathrm{T},h_\mathrm{R})=(0,1)$ (oT-dR) one in the opposite case. A Markov process modeling this behavior can be developed by defining the present state of the network in a generic slot as $\mathbf{s}=(i,o,d)$, where the three indexes i, o, and d represent the number of sources involved in, respectively, an IA stage, a BA stage after an unsuccessful IA one (BA-u), and a BA stage after a successful IA one (BA-s). According to this formalization, the joint coverage probability associated to a

$$F_{P_l^{h_\mathrm{T}h_\mathrm{R}}}(p)=\begin{cases}F_{Q_l}(p) & (h_\mathrm{T},h_\mathrm{R})=(0,0)\\ \omega_l F_{Q_l}\left(\dfrac{p}{\bar{G}}\right)+(1-\omega_l)\,F_{Q_l}\left(\dfrac{p}{\bar{g}}\right) & (h_\mathrm{T},h_\mathrm{R})\in\{(1,0),(0,1)\}\\ \displaystyle\sum_{j,j'=0}^{1}\varepsilon_{ljj'}F_{Q_l}\left(\frac{p}{\chi_{jj'}}\right) & (h_\mathrm{T},h_\mathrm{R})=(1,1)\end{cases} \tag{31a}$$

$$f_{P_l^{h_\mathrm{T}h_\mathrm{R}}}(p)=\begin{cases}f_{Q_l}(p) & (h_\mathrm{T},h_\mathrm{R})=(0,0)\\ \dfrac{\omega_l}{\bar{G}}\,f_{Q_l}\left(\dfrac{p}{\bar{G}}\right)+\dfrac{1-\omega_l}{\bar{g}}f_{Q_l}\left(\dfrac{p}{\bar{g}}\right) & (h_\mathrm{T},h_\mathrm{R})\in\{(1,0),(0,1)\}\\ \displaystyle\sum_{j,j'=0}^{1}\frac{\varepsilon_{ljj'}}{\chi_{jj'}}f_{Q_l}\left(\frac{p}{\chi_{jj'}}\right) & (h_\mathrm{T},h_\mathrm{R})=(1,1)\end{cases} \tag{31b}$$

generic state can be expressed as:

$$\eta^1_{\mathbf{s}}(\upsilon) = \tilde{\eta}^{\mathrm{IA}}_i(\upsilon)\,\tilde{\eta}^{\mathrm{BA-u}}_o(\upsilon)\,\tilde{\eta}^{\mathrm{BA-s}}_d(\upsilon), \tag{35}$$

where:

$$\tilde{\eta}^{\mathrm{IA}}_i(\upsilon) = \eta^{00}_i(\upsilon), \tag{36a}$$

$$\tilde{\eta}^{\mathrm{BA-u}}_o(\upsilon) = \eta^{00}_o(\upsilon), \tag{36b}$$

$$\tilde{\eta}^{\mathrm{BA-s}}_d(\upsilon) = \eta^{01}_d(\upsilon). \tag{36c}$$

The transition from a previous state $\mathbf{s}'$ to a present one $\mathbf{s}$ ($\mathbf{s},\mathbf{s}'\in\mathbb{N}^3$) for an offered load ς may be modeled by a six-dimensional matrix $\mathbf{T}^1(\varsigma,\upsilon)=[T^1_{\mathbf{s}'\mathbf{s}}(\varsigma,\upsilon)]\in[0,1]^6$, whose generic element, by remembering (1) and (3), may be calculated as:

$$T^1_{\mathbf{s}'\mathbf{s}}(\varsigma,\upsilon) = f_I(i;\varsigma)\sum_{k=\tilde{k}_{\mathrm{i}}}^{\tilde{k}_{\mathrm{e}}}\sum_{k'=\tilde{k}'_{\mathrm{i}}}^{\tilde{k}'_{\mathrm{e}}}\left\{\mathcal{B}^{k+k'}_k\left[\eta^1_{\mathbf{s}'}(\upsilon)\right]\right.$$

$$\left.\mathcal{B}^{o'}_{o'-o+k'}\left(\frac{1}{\bar{b}}\right)\mathcal{B}^{i'}_{i'-k-k'}\left(\frac{1}{\bar{b}}\right)\mathcal{B}^{d'}_{d'-d+k}\left(\frac{1}{\bar{b}}\right)\right\}, \tag{37}$$

where $\tilde{k}_{\mathrm{i}}=(d-d')^+$, $\tilde{k}_{\mathrm{e}}=\min(i',d)$, $\tilde{k}'_{\mathrm{i}}=(o-o')^+$, and $\tilde{k}'_{\mathrm{e}}=\min(o',i'-k)$. In this latter formula, the first summation index k refers to the number of pairs that have completed the IA stage and that have further packets to send during the BA one, while the second summation index k' refers to the number of pairs that have completed their burst exchange. Besides, the first binomial function accounts for the coverage probability referred to all active pairs, while the second, third, and fourth binomial functions account for the length of the burst referred, respectively, to the IA stage, and to the BA ones after an unsuccessful and a successful IA stage. A proper elaboration of (37) leads to the following proposition.

Proposition 3 (DirSA-NF Transition matrix): Let the burst length B be distributed according to (2) and the number I of bursts according to (3). Then, for an offered load ς and a SINR threshold υ, the transition probability from a state $\mathbf{s}'$ to a state $\mathbf{s}$ for the DirSA-NF scheme may be written as:

$$T^1_{\mathbf{s}'\mathbf{s}}(\varsigma,\upsilon) = \xi^1_{\mathbf{s}'\mathbf{s}}(\varsigma)\sum_{k=\tilde{k}_{\mathrm{i}}}^{\tilde{k}_{\mathrm{e}}}\binom{i'}{k}\binom{d'}{d-k}\left[\eta^1_{\mathbf{s}'}(\upsilon)\right]^k$$

$$\left\{\sum_{k'=\tilde{k}'_{\mathrm{i}}}^{\tilde{k}'_{\mathrm{e}}}\binom{i'-k}{k'}\binom{o'}{o-k'}\left[1-\eta^1_{\mathbf{s}'}(\upsilon)\right]^{k'}\right\}, \tag{38}$$

where:

$$\xi^1_{\mathbf{s}'\mathbf{s}}(\varsigma) = f_I(i;\varsigma)\,\frac{(\bar{b}-1)^{o+d}}{\bar{b}^{i'+o'+d'}}. \tag{39}$$

Proof: See Appendix H. □

Exploiting the transition matrix, one can estimate the corresponding steady-state probabilities $\boldsymbol{\varphi}^1(\varsigma,\upsilon)=[\varphi^1_{\mathbf{s}}(\varsigma,\upsilon)]\in[0,1]^3$, whose evaluation may be carried out by calculating the left eigenvector, associated to the eigenvalue 1, of $\mathbf{T}^1(\varsigma,\upsilon)$ [32].

This, in turn, allows the calculation of the throughput as:

$$S = S(\varsigma,\upsilon) = \mathcal{E}_1(\bar{b})\,\varrho_m(\upsilon)\sum_{\mathbf{s}\in\mathbb{N}^3}\varphi^1_{\mathbf{s}}(\varsigma,\upsilon)\,\langle\mathbf{s},\boldsymbol{\eta}^1_{\mathbf{s}}(\upsilon)\rangle, \tag{40}$$

where $\mathcal{E}_1(\bar{b})$ is given by (34), $\varrho_m(\upsilon)$ by (9), and:

$$\boldsymbol{\eta}^1_{\mathbf{s}}(\upsilon) = [\tilde{\eta}^{\mathrm{IA}}_i(\upsilon),\tilde{\eta}^{\mathrm{BA-u}}_o(\upsilon),\tilde{\eta}^{\mathrm{BA-s}}_d(\upsilon)]. \tag{41}$$

Since (40) is obtained by multiplying the selected rate with the average successfully transmitted packets per slot, the throughput, similarly to $\varrho_m(\upsilon)$, may be expressed in information bits per transmission. Besides, the absence of feedback implies that the actual load entering in the system:

$$\varsigma_{\mathrm{a}} = \varsigma_{\mathrm{a}}(\varsigma) = \varsigma\bar{b}, \tag{42}$$

is directly proportional to the offered one, since each active pair attempts to accomplish the exchange of the burst independently of the result of the IA stage.

B. DirSA-F

When the feedback mechanism is available, a successful IA stage requires that an $(h_{\mathrm{T}},h_{\mathrm{R}})=(0,0)$ (oT-oR) communication type and an $(h_{\mathrm{T}},h_{\mathrm{R}})=(1,0)$ (dT-oR) one are both successful. If this event occurs, the BA stage begins adopting an $(h_{\mathrm{T}},h_{\mathrm{R}})=(1,1)$ (dT-dR) communication type. The Markov chain modeling this access mechanism may be derived by identifying the present state of the network as $\mathbf{s}=(i,d)$, where i and d denote the number of sources involved in an IA stage and a BA one, respectively. By consequence, the joint coverage probability associated to $\mathbf{s}$ becomes:

$$\eta^2_{\mathbf{s}}(\upsilon) = \hat{\eta}^{\mathrm{IA}}_i(\upsilon)\,\hat{\eta}^{\mathrm{BA}}_d(\upsilon), \tag{43}$$

where:

$$\hat{\eta}^{\mathrm{IA}}_i(\upsilon) = \eta^{00}_i(\upsilon)\,\eta^{10}_i(\upsilon), \tag{44a}$$

$$\hat{\eta}^{\mathrm{BA}}_d(\upsilon) = \eta^{11}_d(\upsilon). \tag{44b}$$

The modeling of the transition from a previous state $\mathbf{s}'$ to a present one $\mathbf{s}$ ($\mathbf{s},\mathbf{s}'\in\mathbb{N}^2$) now requires the usage of a four-dimensional matrix $\mathbf{T}^2(\varsigma,\upsilon)=[T^2_{\mathbf{s}'\mathbf{s}}(\varsigma,\upsilon)]\in[0,1]^4$, whose generic element can be determined as:

$$T^2_{\mathbf{s}'\mathbf{s}}(\varsigma,\upsilon) = f_I(i;\varsigma)\sum_{k=\hat{k}_{\mathrm{i}}}^{\hat{k}_{\mathrm{e}}}\sum_{k'=0}^{i'-k}\left\{\mathcal{B}^{k+k'}_k\left[\eta^2_{\mathbf{s}'}(\upsilon)\right]\right.$$

$$\left.\mathcal{B}^{i'}_{i'-k-k'}\left(\frac{1}{\bar{b}}\right)\mathcal{B}^{d'}_{d'-d+k}\left(\frac{1}{\bar{b}}\right)\right\}, \tag{45}$$

where $\hat{k}_{\mathrm{i}}=\tilde{k}_{\mathrm{i}}$, $\hat{k}_{\mathrm{e}}=\min(i',d)$, and the two summation indexes as well as the first binomial function maintain the same meaning previously explained for (37). The second and third binomial functions account for the length of the burst referred to the IA and BA stages, respectively. Similarly to the previous case, also (45) can be elaborated to formulate the following proposition.

Proposition 4 (DirSA-F Transition matrix): Let the burst length B be distributed according to (2) and the number I of bursts according to (3). Then, for an offered load ς and a SINR

threshold υ, the transition probability from a state $\mathbf{s}'$ to a state $\mathbf{s}$ for the DirSA-F scheme may be written as:

$$T^2_{\mathbf{s}'\mathbf{s}}(\varsigma,\upsilon)=\xi^2_{\mathbf{s}'\mathbf{s}}(\varsigma)\sum_{k=\hat{k}_\mathrm{i}}^{\hat{k}_\mathrm{e}}\frac{\binom{i'}{k}\binom{d'}{d-k}\left[\eta^2_{\mathbf{s}'}(\upsilon)\right]^k}{\left[\bar{b}-(\bar{b}-1)\hat{\eta}_{\mathbf{s}'}(\upsilon)\right]^k}, \tag{46}$$

where:

$$\xi^2_{\mathbf{s}'\mathbf{s}}(\varsigma)=f_I(i;\varsigma)\frac{(\bar{b}-1)^d}{\bar{b}^{i'+d'}}\left[\bar{b}-(\bar{b}-1)\eta^2_{\mathbf{s}'}(\upsilon)\right]^{i'}. \tag{47}$$

Proof: See Appendix I. □

Once the transition matrix is characterized, the corresponding steady-state probabilities $\boldsymbol{\varphi}^2(\varsigma,\upsilon)=[\varphi^2_{\mathbf{s}}(\varsigma,\upsilon)]\in[0,1]^2$ enable the estimation of the throughput as:

$$S=S(\varsigma,\upsilon)=\mathcal{E}_2(\bar{b})\,\varrho_m(\upsilon)\sum_{\mathbf{s}\in\mathbb{N}^2}\varphi^2_{\mathbf{s}}(\varsigma,\upsilon)\,\langle\mathbf{s},\boldsymbol{\eta}^2_{\mathbf{s}}(\upsilon)\rangle, \tag{48}$$

where:

$$\boldsymbol{\eta}^2_{\mathbf{s}}(\upsilon)=[\hat{\eta}^{\mathrm{IA}}_i(\upsilon),\hat{\eta}^{\mathrm{BA}}_d(\upsilon)]. \tag{49}$$

Note that, according to (44a), the first vector component in (49), representing the coverage probability for the IA stage, properly accounts for the two required successful $(h_\mathrm{T},h_\mathrm{R})=(0,0)$ and $(h_\mathrm{T},h_\mathrm{R})=(1,0)$ communication types. The actual load entering in the system can be in this case evaluated as:

$$\varsigma_\mathrm{a}=\varsigma_\mathrm{a}(\varsigma,\upsilon)=\sum_{\mathbf{s}\in\mathbb{N}^2}\varphi^2_{\mathbf{s}}(\varsigma,\upsilon)||\mathbf{s}||_1, \tag{50}$$

which, differently from (42), is not directly proportional to ς and is also a function of the SINR value. This behavior is specifically due to the presence of the feedback mechanism, which reduces the number of packets entering in the system with respect to the number of generated ones, since the access to the BA stage is reserved to the sole pairs that have successfully completed the IA one.

V. Results

This section discusses the results obtained from the developed P2P DirSA model by also checking its accuracy though independent Monte Carlo simulations. Both the analytical formulas and the validation routines are implemented in Matlab, assuming propagation contexts in agreement with the recent proposals for the 6G scenario. The presentation of the results is organized in two parts by firstly considering, in the following subsection, the coverage aspects and subsequently, in Section V-B, the throughput ones.

A. Coverage Probability

The adopted coverage parameters are reported in Table II. In particular, the cell radius refers to a femtocell [4], [29], [30], while the path-loss, shadowing, and bandwidth parameters to measurements carried out in the 28 GHz mmWave band [29, Table I]. To guarantee a fair comparison among the three contexts, line-of-sight (LoS) propagation is assumed, with moderate fading [30], and scintillation [31, Table I], for the air and space environments, respectively. The noise figure [18], as well as the antenna beamwidth, backlobe and maximum gains [33], are chosen to model very simple transceivers, suitable for low-cost IoT devices. A partial insolation has been assumed for the satellites [4], thus considering a receiver temperature some dozens of degrees higher than the room one that typically characterizes the gound/air nodes. Besides, to speed up the numerical integration of (33) for $n\geq 2$, the variable p is exponentially discretized, while each point of a simulated curve is obtained by averaging over $M=10^5$ realizations.

TABLE II
Coverage Parameters [29], [30], [31]

General					
ρ	50 m	$\bar{g}$	-5 dB	W_R	1 GHz
P_T	100 mW	α_1	61.4 dB	$\mathcal{F}_\mathrm{R}$	10 dB
$\bar{G}$	5 dB	α_2	2	$\Omega=3\hat{\sigma}$	$\pi/6$ rad (sr)
Ground		Air		Space	
T_R	288 K	T_R	288 K	T_R	323 K
$\tilde{\sigma}$	5.8 dB	μ_1	2	μ_1	4
				μ_2	1

The first set of results is presented in Fig. 2, which shows the coverage probability as a function of the SINR for different numbers of contending pairs when the oT-dR or dT-oR communication type is assumed and the ground (Fig. 2(a)), air (Fig. 2(b)), and space (Fig. 2(c)) environments are considered. The theoretical curves are plotted by lines, while the simulations are identified by markers. As expected, for a given context and a given υ value, the increase of n leads to a reduction of the coverage probability. When the number of interferers is large, however, this reduction is not so strong as to completely inhibit the communications. In fact, even in the case $n=20$, not negligible $\eta^{10}_n(\upsilon)=\eta^{01}_n(\upsilon)$ values may be achieved by choosing the operating SINR in the interval [-5,0] dB, a range that is nowadays assumed sufficient to sustain many basic code-modulation schemes supported by last generation terrestrial, aerial, and satellite receivers. This aspect is interesting also in light of the adopted antenna parameters (Table II), which have been deliberately selected to offer limited capabilities in terms of main lobe and backlobe gains. This choice has been in fact carried out in line with the expected weight, size, and energy constraints that will reasonably characterize the 6G P2P nodes, with subnets possibly consisting of miniaturized sensors/actuators, micro/nano-UAVs, and pico/femto-satellites.

The second set of results is illustrated in Fig. 3, which reports the coverage probability as a function of the SINR for $n=5$ pairs considering all the different contexts and communication types. In this case, the curves are organized in three sets, corresponding to the oT-oR, dT-oR (or oT-dR), and dT-dR types, to better clarify, for a given environment, the benefits fostered by an increasingly directional link. Just this latter aspect is targeted by the DirSA approach, which, moving from an omnidirectional transmission/reception, aims to achieve at least a directional reception in the absence of feedback, and a fully directional exchange when the feedback is instead enabled. Still from the coverage point of view, more insights concerning the differences between

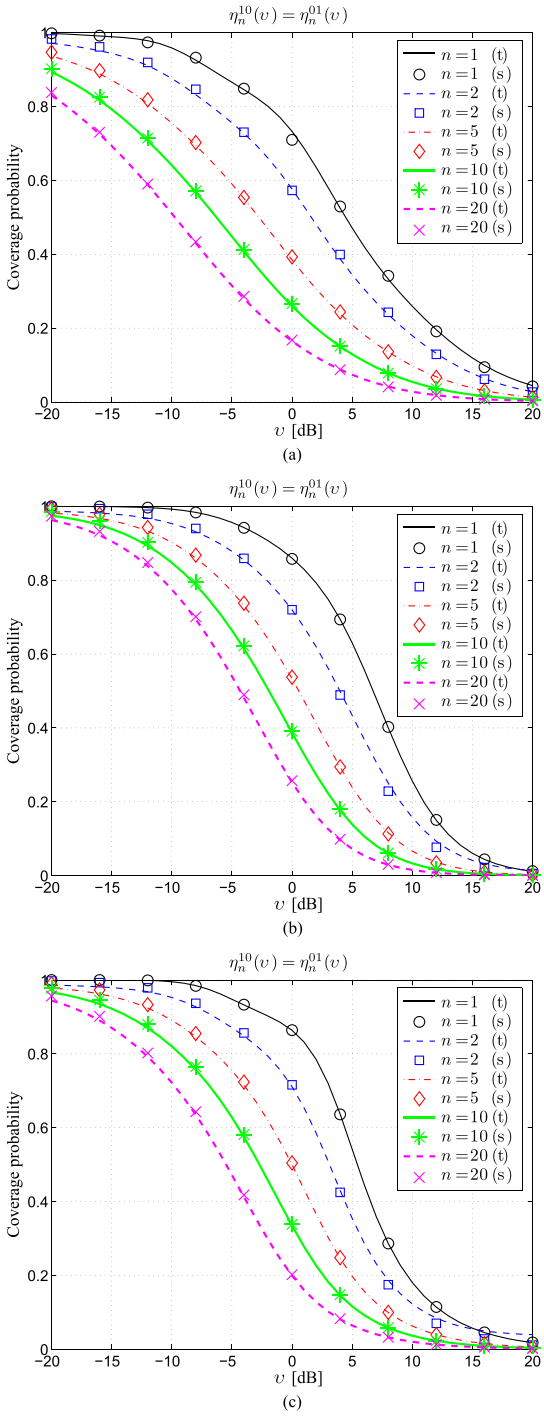

Fig. 2. Coverage probability as a function of the SINR for $(h_{\mathrm{T}},h_{\mathrm{R}})\in\{(1,0),(0,1)\}$ and different numbers of contending pairs: (a) Ground, (b) air, (c) space (t: Theory, s: Simulation).

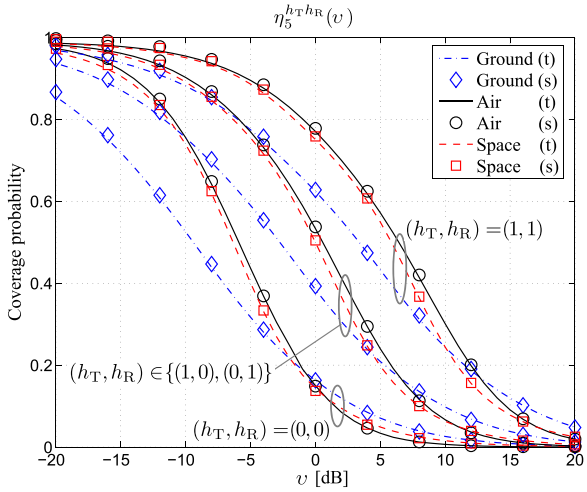

Fig. 3. Coverage probability as a function of the SINR for $n=5$ considering different communication types and propagation contexts (t: Theory, s: Simulation).

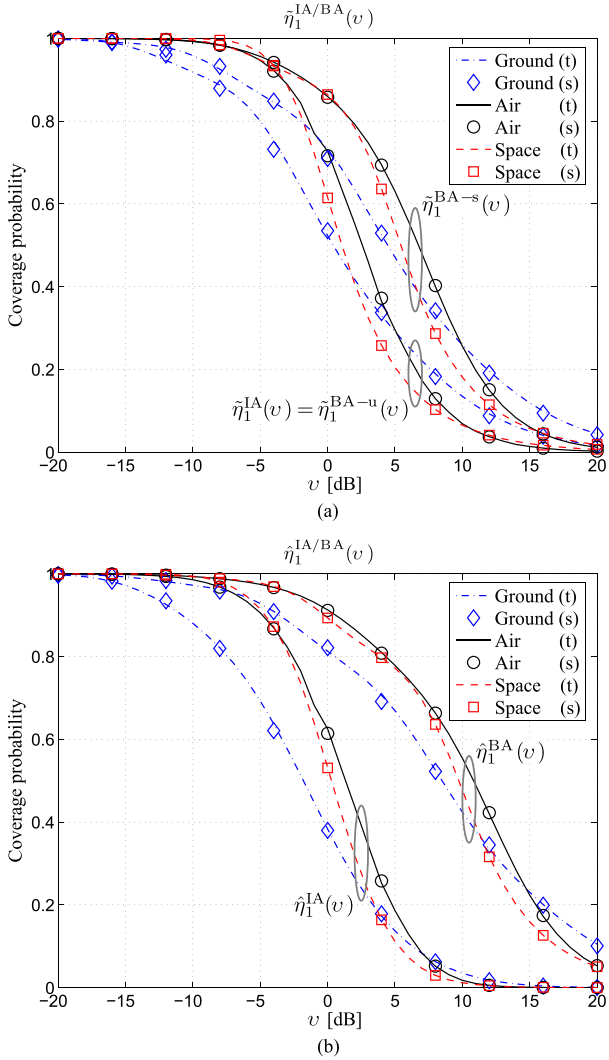

Fig. 4. Coverage probability referred to the IA and BA stages as a function of the SINR for $n=1$ and different propagation contexts: (a) DirSA-NF, (b) DirSA-F (t: Theory, s: Simulation).

the two options may be inferred from Fig. 4. This figure shows in fact, for $n=1$ and different propagation contexts, the coverage probability specifically referred to the IA and BA stages in the absence (Fig. 4(a)) and in the presence (Fig. 4(b)) of feedback, according to the formulas in (36) and (44), respectively. By directly comparing the two sets of curves corresponding to the pair $[\tilde{\eta}_1^{\mathrm{IA}}(\upsilon),\tilde{\eta}_1^{\mathrm{BA-s}}(\upsilon)]$ with those corresponding to the pair

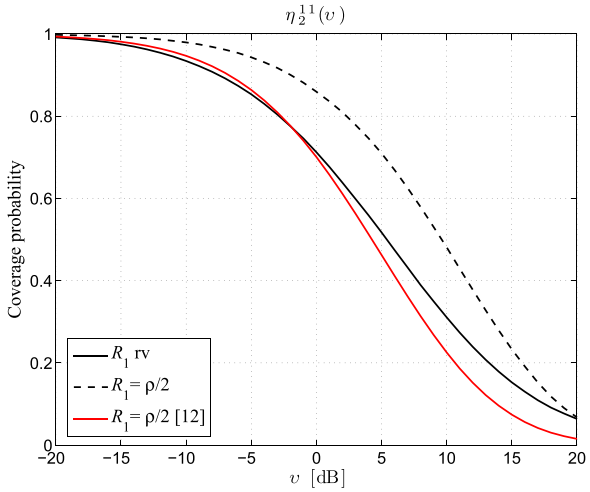

Fig. 5. Theoretical coverage probability as a function of the SINR in the ground context for $n=2$, $(h_{\mathrm{T}}, h_{\mathrm{R}})=(1,1)$, and $\alpha_2=2.1$: comparison between the analysis in [12] and the proposed one with random and fixed $\mathrm{S}-\mathrm{D}$ distances.

$[\hat{\eta}_1^{\mathrm{IA}}(\upsilon), \hat{\eta}_1^{\mathrm{BA}}(\upsilon)]$, one may preliminarily infer some advantages and drawbacks of each option before the detailed throughput discussion illustrated in the next subsection. More precisely, for a given context, a successful IA stage is more likely to occur in a DirSA-NF scheme, since, adopting the other option, the same stage requires that, beside the first oT-oR communication, also the subsequent dT-oR one be successful. On the other hand, thanks to the fully directional link, the BA stage of the DirSA-F scheme is characterized by a coverage probability considerably higher than that achievable by the DirSA-NF one, even if the oT-dR communication is enabled. In synthesis, as compared to the DirSA-NF option, the DirSA-F one is characterized by a more selective IA stage, which is however highly compensated by a much more reliable BA one. This behavior might also be guessed at a glance by observing that the $\tilde{\eta}_1^{\mathrm{IA}}(\upsilon)$ and $\tilde{\eta}_1^{\mathrm{BA-s}}(\upsilon)$ sets of curves are, among them, much closer than the $\hat{\eta}_1^{\mathrm{IA}}(\upsilon)$ and $\hat{\eta}_1^{\mathrm{BA}}(\upsilon)$ ones. Beside the differences between the DirSA options, Fig. 4 shows also those due to the propagation context. In particular, given an option and a stage, the air context provides a coverage probability higher than that achieved in the other two environments in the low to medium SINR regime. Aerial P2P networks, in fact, generally operate in a 3D domain, where the interferers result spread over a region wider than the 2D one covered by terrestrial and spatial subnets, whose nodes have to typically move on the Earth surface or on predefined orbits.

As a final result for this subsection, Fig. 5 illustrates a comparison between the coverage analysis in [12, Eqs. (18)–(21)] and the present one, which is carried out in the ground context for $n=2$ and $(h_{\mathrm{T}}, h_{\mathrm{R}})=(1,1)$ (i.e., dT-dR communication type). For fairness reasons, the comparing curves are evaluated for a unity packet generation probability and a $\lambda/2$ Poisson intensity, since in the present coverage model the interferer is surely active and λ, given by (12), is referred to the pairs, while, in [12], it is referred to the nodes (i.e., both transmitters and receivers). The remaining parameters are chosen in agreement with Table II, except for the path-loss exponent $\alpha_2=2.1$, whose value is selected to avoid the divergence point of the cosecant function in [12, Eq. (18)]. Moreover, to clarify the difference between fixed and random $\mathrm{S}-\mathrm{D}$ distances, the figure also reports the curve derived from the proposed analysis but constrained to the same $R_1=\rho/2$ value used for computing [12, Eqs. (18)–(21)]. This latter curve theoretically confirms an aspect investigated by simulations in [16]. In particular, as compared to the fixed $\mathrm{S}-\mathrm{D}$ distance, the random one provides a quite conservative performance when the same channel/antenna model is adopted, since, in this second case, the closeness between the communicating nodes depends on the single rv realization. Interestingly, the coverage probabilities evaluated using the proposed analysis and that in [12] show a considerable agreement, even if they derive from two distinct mathematical approaches. Beside the usage of random and fixed $\mathrm{S}-\mathrm{D}$ distances, the residual differences between the two models may be due to the additional presence of Rayleigh fading and the evaluation of the interference in the entire $\mathbb{R}^2$ space carried out in [12], in place of the here assumed nearest neighbor approximation in (13).

B. Throughput

The throughput results are derived maintaining the parameters in Table II and assuming $\tau_{\mathrm{H}}/\tau=0.05$. Besides, the quantities in (35)–(41) and (43)–(50) are estimated by considering $i,o,d\leq N=20$ to reasonably limit the computational cost. Monte Carlo simulations are again carried out to validate this choice. In particular, with reference to the values discussed in the previous section, the theoretical throughput is calculated using the analytical coverage probabilities, while its validation is obtained employing the simulated $\eta_n^{h_{\mathrm{T}}h_{\mathrm{R}}}(\upsilon)$ values.

Fig. 6 shows the throughput as a function of the actual load achieved by the DirSA-NF and DirSA-F schemes for $m=0$, $\upsilon=0$ dB, and different burst lengths in the ground (Fig. 6(a)), air (Fig. 6(b)), and space (Fig. 6(c)) contexts. For comparison purposes, the figure also reports the performance of the SA protocol with capture, corresponding to the selection of $\bar{b}=1$ and no overhead, since the exchange of a single-packet burst involves a unique oT-oR communication type. This figure puts immediately into evidence the capability of the DirSA-F option to benefit from the increase of the burst length, while the DIRSA-NF one remains almost insensitive to this parameter. Both behaviors derive from the functionalities of the two access mechanisms. In particular, in DirSA-F, when the IA stage is successful, the rest of the burst becomes significantly protected from the interference, thus the presence of a longer burst implies more successful packets and hence a higher throughput. Conversely, in DIRSA-NF, even after a successful IA stage, the protection from the interference is limited, since in any case all pairs go on transmitting their packets during the BA stage, thus leading to a small influence of the burst length on the throughput. Beside the impact of $\bar{b}$, the results in the figure reveal two further interesting aspects. A first one, quite expected, puts into evidence that, for a given context and a given $\bar{b}$ value, the DirSA-F throughput typically achieves a higher maximum with respect to the DIRSA-NF one. The second aspect, somewhat surprising and more evident from the ground context for low $\bar{b}$ values, concerns the better performance of the DirSA-NF solution for high loads. This behavior is specifically due to the possibility, left

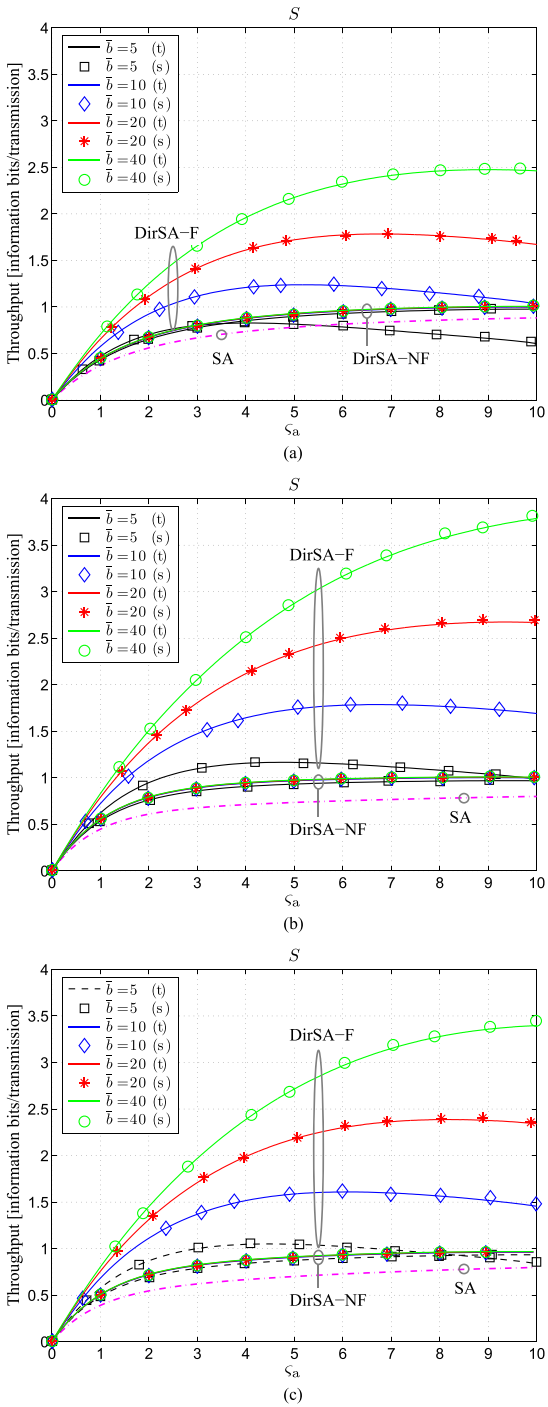

Fig. 6. Throughput as a function of the actual load referred to the DirSA-NF and DirSA-F options for $m=0$, $\upsilon=0$ dB, and different burst lengths: (a) Ground, (b) air, (c) space (t: Theory, s: Simulation).

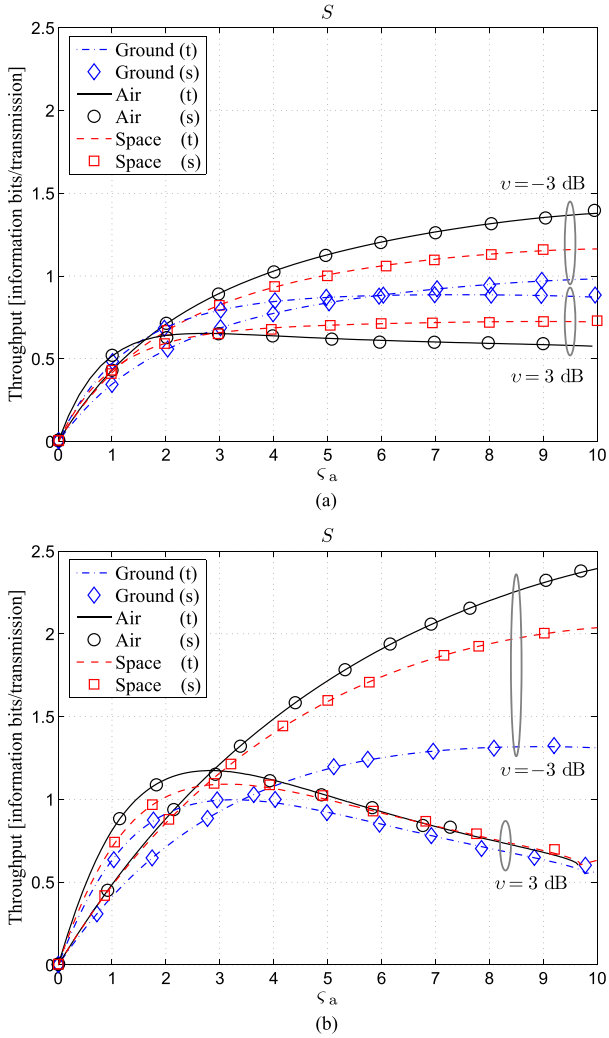

Fig. 7. Throughput as a function of the actual load for $m=0$ and $\bar{b}=10$ considering different SINR values and propagation contexts: (a) DirSA-NF, (b) DirSA-F (t: Theory, s: Simulation).

by the no feedback option, of attempting the transmission of all packets of the burst also to the sources that have experienced an unsuccessful IA stage ($\varsigma_a=\varsigma\bar{b}$). When the actual load becomes significant, this leads to a high number of attempts, which, even for low coverage probabilities, may determine a not negligible contribution to the overall throughput. Conversely, the DirSA-F policy of limiting the access to the BA stage to the sole sources that have passed the IA one ($\varsigma_a<\varsigma\bar{b}$), considerably reduces the number of attempts, finally determining, for a sufficiently high load, a performance sometimes lower than that of the DirSA-NF scheme. This result, showing the preferability of a reduced coordination (DirSA-NF) in some situations, might be seen as complementary to that proved in [14], indicating the coordination loss due to erroneous beam pointings as more harmful than the interference loss due to excessive loads. From the context perspective, Fig. 6 confirms the higher throughput achievable by air and space P2P networks with respect to terrestrial subnets. A result partly expected, recalling the coverage curves in Fig. 4 and the selected $\upsilon=0$ dB threshold, which, for almost all stages, lead to coverage probabilities for the air and space contexts close to each other and higher than those corresponding to the ground environment.

Fig. 7 focuses on the impact of the SINR threshold by reporting, for $m=0$ and $\bar{b}=10$, the throughput of the DirSA-NF (Fig. 7(a)) and DirSA-F (Fig. 7(b)) options as a function of the actual load in different propagation contexts. This figure shows that lower and higher υ values may be preferable in the presence

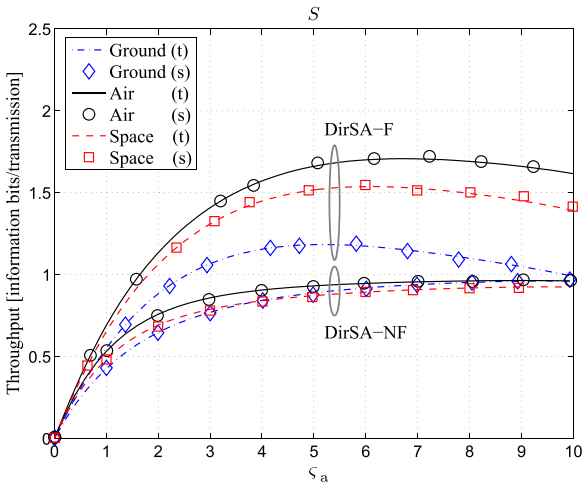

Fig. 8. Throughput as a function of the actual load referred to the DirSA-NF and DirSA-F options for $m=1$, $\upsilon=0$ dB, and $\bar{b}=10$ considering different propagation contexts (t: Theory, s: Simulation).

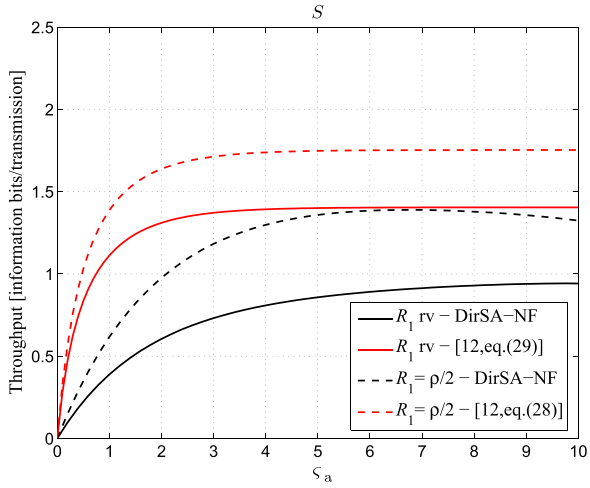

Fig. 9. Theoretical throughput as a function of the actual load in the ground context for $\alpha_2=2.1$, $m=0$, $\upsilon=0$ dB, and $\bar{b}=10$: Comparison between the analysis in [12] and the proposed one for the DirSA-NF option with random and fixed S − D distances.

of, respectively, lower and higher loads, while, for higher SINR thresholds, the choice between the feedback and no feedback option is still dependent on the actual load and the propagation context. Concerning this last aspect, one may observe that, using the DirSA-F option with $\upsilon=3$ dB, a similar throughput is achieved in the three contexts. This behavior may be again inferred from the coverage curves, by specifically noticing from Fig. 4(b) that close $\hat{\eta}_1^{\mathrm{IA}}(\upsilon)$ values are obtained for $\upsilon=3$ dB. Since the so far presented throughput results were referred to the Shannon bound ($m=0$), it may be interesting to observe their variation when a more realistic LDPC/QPSK code-modulation pair is adopted. To this aim, Fig. 8 illustrates the DirSA-NF and DirSA-F throughput as a function of the actual load for $m=1$, $\upsilon=0$ dB, $\bar{b}=10$, and different propagation contexts. A direct comparison of each curve in this figure with the corresponding one plotted in Fig. 6, shows that the usage of a practical, but efficient, code-modulation scheme determines just a moderate reduction of the performance with respect to the ideal case. As a final comment concerning the reported throughput results, one may notice that, in agreement with [12] and [15], those referred to the DirSA-F scheme usually exhibit a quite clear maximum. Differently, those referred to the DirSA-NF option reveal a definitely flatter trend once the maximum is reached. This is again due to the probabilistic coverage model, which, in high load conditions, leaves a residual success opportunity to a large number of nodes regardless of the initial access outcome.

Similarly to what done at the end of the previous subsection, Fig. 9 reports a comparison between the throughput analysis in [12, Eqs. (18)–(21), (28)–(29)] and the present one referred to the DirSA-NF option by considering fixed and random S − D distances in the ground context. The results are derived for $m=0, \upsilon=0$ dB, $\bar{b}=10$, again applying the values in Table II with the previous observations on α_2 and λ. The throughput formula in [12, Eq. (28)], which relies on the dipole model, and that [12, Eq. (29)], which instead relies on a random S − D distance, are both normalized with respect to λ and multiplied by $\bar{b}$ to have a measurement unit congruent with that adopted in the proposed analysis. Furthermore, still with reference to [12], the oT-dR communication type with ready receivers is assumed, while the packet generation probability is selected equal to $1-f_I(0;\varsigma)$, with $f_I(i;\varsigma)$ given by (3), to enable the comparability between the theoretical models and the agreement with the DirSA-NF operations. The figure confirms, for a given analysis, the conservative performance provided by the random S − D distance with respect the fixed one, which was already observed through the coverage results. Moreover, for a given distance model, the framework in [12] leads to a throughput higher than that provided by the DirSA-NF option. This behavior may be reasonably charged to the assumption in [12] of pre-aligned beams, which neglects the antenna pointing operations instead included in the presented analysis through the IA stage.

VI. Conclusion

A mathematical framework for evaluating the performance of 6G P2P DirSA networks in ground, air, and space propagation contexts with Poisson bursty traffic has been presented. The conceived theoretical analysis, which accounts for interference, noise, path-loss, random node location, power fluctuation, antenna pointing error, transmission/reception mode, and beamforming training overhead, has been derived to investigate the influence of directionality and feedback response on the evolution of a random access subnet. Closed-form expressions for the received power and simple integral formulas for the coverage probability have been obtained to subsequently enable the throughput estimation by developing suitable multidimensional Markov chain models.

The analytical and numerical results have shown that, in all considered environments, the benefits of directional communications may be better exploited by the DirSA-F option for long bursts and low to moderate loads. However, even if the highest throughput values may be achieved in the presence of the feedback mechanism, in some propagation contexts the

DirSA-NF scheme can become preferable for high channel loads and low burst lengths. In phase of possible implementation, this limited uncertainty might be addressed by observing that, as compared to the typical SA scheme, the DirSA one requires just minimal modifications, consisting in the addition, at the PHY layer, of a beam-steering antenna system and, at the MAC layer, of a single header field and an optional feedback packet. Besides, the applicability of the analyzed DirSA schemes in next-generation P2P subnets is fostered by the adoption of the mmWave domain, which allows one to equip each node with an antenna array, thanks to the reduced dimensions of the single radiating element. Furthermore, similarly to the WiFi switching from a basic to a reserved access, a simple adaptive strategy relying on a properly configured parameter may enable each contending pair to choose between the DirSA-F and the DirSA-NF options. A reasonable combination of this latter feature with the by now almost standard IC and packet diversity ones, is one of the objectives of current research efforts for applying the proposed analysis to 6G uncoordinated ultra-dense networks.

APPENDIX

A. Proof of Lemma 1

The cases $(h_{\mathrm{T}},h_{\mathrm{R}})=(0,0)$ and $(h_{\mathrm{T}},h_{\mathrm{R}})\in\{(1,0),(0,1)\}$ in (21) respectively coincide with the cases $h=0$ and $h=1$ in (7), since at least one of the two multiplied gains is unitary. For $(h_{\mathrm{T}},h_{\mathrm{R}})=(1,1)$, apply the product distribution [24], substitute (7), and exploit the translation and scaling properties of the delta function. Recalling (22a), this yields:

$$\begin{aligned} f_{G_l^{11}}(g) &= \int_{-\infty}^{+\infty} f_{G_{\mathrm{T}_l}^{1}}(g') f_{G_{\mathrm{R}_l}^{1}}\left(\frac{g}{g'}\right)\frac{\mathrm{d}g'}{g'} \\ &= \sum_{j,j'=0}^{1}\varepsilon_{ljj'}\int_{-\infty}^{+\infty}\delta\left(g'-\frac{\bar{g}^{j}}{\bar{G}^{j-1}}\right)\delta\left(\frac{g}{g'}-\frac{\bar{g}^{j'}}{\bar{G}^{j'-1}}\right)\frac{\mathrm{d}g'}{g'} \\ &= \sum_{j,j'=0}^{1}\varepsilon_{ljj'}\delta\left(\frac{g\bar{G}^{j-1}}{\bar{g}^{j}}-\frac{\bar{g}^{j'}}{\bar{G}^{j'-1}}\right)\frac{\bar{G}^{j-1}}{\bar{g}^{j}} \\ &= \sum_{j,j'=0}^{1}\varepsilon_{ljj'}\delta\left(g-\frac{\bar{g}^{j'}}{\bar{G}^{j'-1}}\frac{\bar{g}^{j}}{\bar{G}^{j-1}}\right), \end{aligned} \tag{51}$$

from which, using (22b), one obtains the third case in (21).

B. Proof of Lemma 2

Define the rv $T_l=\theta/R_l^{\alpha_2}$, which, being invertible, allows the evaluation of the corresponding cdf as:

$$F_{T_l}(t)=\Pr\{T_l\le t\}=1-F_{R_l}\left[\left(\frac{\theta}{t}\right)^{\frac{1}{\alpha_2}}\right]. \tag{52}$$

The usage of (13) in (52) and of (26d) provides:

$$F_{T_l}(t)=\exp\left[-\pi\lambda\left(\frac{\theta}{t}\right)^{\beta^{\mathrm{t}}}\right]\mathbb{1}_{\mathbb{R}_{>0}}(t). \tag{53}$$

Hence, Q_l can be redefined as $T_l\Psi_l$, whose cdf is given by the product distribution:

$$F_{Q_l}(q)=\int_{-\infty}^{+\infty}F_{T_l}\left(\frac{q}{\psi}\right)f_{\Psi_l}(\psi)\,\mathrm{d}\psi. \tag{54}$$

Since, in this case, (54) does not provide closed-forms, the approximation adopted in [18], which holds for normal and log-normal rvs, is applied. Accordingly, the integral in (54) is approximated by:

$$F_{Q_l}(q)\cong\frac{2}{3}\sum_{k\in\mathbb{D}^{\mathrm{t}}}\frac{1}{4^{|k|}}F_{T_l}\left[\frac{q}{\exp\left(\sqrt{3}\,\tilde{\sigma}k\right)}\right], \tag{55}$$

from which, by using (53) and the other definitions in (26), one obtains (25a), whose derivative leads to (25b).

C. Proof of Lemma 3

Similarly to *Lemma 2*, substitute (15) in (52) recalling (28d) and (28e). This yields:

$$F_{T_l}(t)=-\left[\sum_{k\in\mathbb{D}^{\mathrm{a}}}a_k\left(\frac{c^{\mathrm{a}}}{t}\right)^{\beta_k^{\mathrm{a}}}\right]\mathbb{1}_{[c^{\mathrm{s}},+\infty[}(t), \tag{56}$$

which, once inserted in (54) together with (16) and (28a), leads to the integral:

$$\begin{aligned} F_{Q_l}(q)=\mu_1^{\mu_1}\sum_{k\in\mathbb{D}^{\mathrm{a}}}A_k^{\mathrm{a}}\left(\frac{\mu_1}{q}\right)^{\beta_k^{\mathrm{a}}} \\ \cdot\int_0^{\frac{q}{c^{\mathrm{a}}}}\psi^{\beta_k^{\mathrm{a}}+\mu_1-1}\exp\left(-\mu_1\psi\right)\,\mathrm{d}\psi, \end{aligned} \tag{57}$$

whose resolution, applying the other definitions in (28), provides (27a) and, by a subsequent derivation, (27b).

D. Proof of Lemma 4

Similarly to *Lemma 2*, insert (17) in (52) recalling (30d) and (30e), thus obtaining:

$$F_{T_l}(t)=\left[\sum_{k\in\mathbb{D}^{\mathrm{s}}}(-1)^k\left(\frac{c^{\mathrm{s}}}{t}\right)^{\beta_k^{\mathrm{s}}}\right]\mathbb{1}_{[c^{\mathrm{s}},+\infty[}(t). \tag{58}$$

Substituting (18) and (58) in (54) and then remembering (30a), one derives the integral:

$$\begin{aligned} F_{Q_l}(q)=\frac{\mu_2}{\mu_3^{\mu_1\mu_2}}\sum_{k\in\mathbb{D}^{\mathrm{s}}}A_k^{\mathrm{s}}\left(\frac{\mu_1}{q}\right)^{\beta_k^{\mathrm{s}}} \\ \cdot\int_0^{\frac{q}{c^{\mathrm{s}}}}\psi^{\beta_k^{\mathrm{s}}+\mu_1\mu_2-1}\exp\left[-\left(\frac{\psi}{\mu_3}\right)^{\mu_2}\right]\mathrm{d}\psi, \end{aligned} \tag{59}$$

which, once resolved and manipulated using the other definitions in (30), leads to (29a), whose derivative provides (29b).

E. Proof of Proposition 1

Apply the product distribution to the definition of $P_l^{h_{\mathrm{T}}h_{\mathrm{R}}}$ in (23). This yields:

$$F_{P_l^{h_{\mathrm{T}}h_{\mathrm{R}}}}(p)=\int_{-\infty}^{+\infty}F_{Q_l}\left(\frac{p}{g}\right)f_{G_l^{h_{\mathrm{T}}h_{\mathrm{R}}}}(g)\,\mathrm{d}g, \tag{60}$$

from which, by substituting (21) and exploiting the translation property of the delta function, one derives (31a), whose derivative leads to (31b).

F. Proof of Proposition 2

For $n=1$, (32) becomes $\Upsilon_n^{h_{\mathrm{T}}h_{\mathrm{R}}}=P_1^{h_{\mathrm{T}}h_{\mathrm{R}}}/\mathcal{N}$, thus the cdf is directly obtained from the scaling rule for rvs [24]. For $n\geq 2$, the strongest interferer approximation allows the estimation of the undesired power as [18]:

$$U_n^{h_{\mathrm{T}}h_{\mathrm{R}}}=\sum_{l=2}^{n}P_l^{h_{\mathrm{T}}h_{\mathrm{R}}}+\mathcal{N}\cong\max_{2\leq l\leq n}\left\{P_l^{h_{\mathrm{T}}h_{\mathrm{R}}}\right\}+\mathcal{N}, \tag{61}$$

whose cdf, recalling the rules for the maximum and the translation of rvs [24], is given by:

$$F_{U_n^{h_{\mathrm{T}}h_{\mathrm{R}}}}(u)\cong F^{n-1}_{P_{l\geq 2}^{h_{\mathrm{T}}h_{\mathrm{R}}}}(u-\mathcal{N}). \tag{62}$$

Redefine now the SINR in (32) as:

$$\Upsilon_n^{h_{\mathrm{T}}h_{\mathrm{R}}}=P_1^{h_{\mathrm{T}}h_{\mathrm{R}}}Y_n^{h_{\mathrm{T}}h_{\mathrm{R}}}, \tag{63}$$

where the cdf of the rv $Y_n^{h_{\mathrm{T}}h_{\mathrm{R}}}=1/U_n^{h_{\mathrm{T}}h_{\mathrm{R}}}$ is evaluated employing the inverse distribution [24] and then (62) as:

$$F_{Y_n^{h_{\mathrm{T}}h_{\mathrm{R}}}}(y)=1-F_{U_n^{h_{\mathrm{T}}h_{\mathrm{R}}}}\left(\frac{1}{y}\right)\cong 1-F^{n-1}_{P_{l\geq 2}^{h_{\mathrm{T}}h_{\mathrm{R}}}}\left(\frac{1}{y}-\mathcal{N}\right). \tag{64}$$

The coverage probability, given by the ccdf of $\Upsilon_n^{h_{\mathrm{T}}h_{\mathrm{R}}}$, is calculated from the product distribution and using (64) as:

$$\begin{aligned}\eta_n^{h_{\mathrm{T}}h_{\mathrm{R}}}(\upsilon)&=1-F_{\Upsilon_n^{h_{\mathrm{T}}h_{\mathrm{R}}}}(\upsilon)\\&=1-\int_{-\infty}^{+\infty}F_{Y_n^{h_{\mathrm{T}}h_{\mathrm{R}}}}\left(\frac{\upsilon}{p}\right)f_{P_1^{h_{\mathrm{T}}h_{\mathrm{R}}}}(p)\,\mathrm{d}p\\&\cong 1-\int_{-\infty}^{+\infty}\left[1-F^{n-1}_{P_{l\geq 2}^{h_{\mathrm{T}}h_{\mathrm{R}}}}\left(\frac{p}{\upsilon}-\mathcal{N}\right)\right]f_{P_1^{h_{\mathrm{T}}h_{\mathrm{R}}}}(p)\,\mathrm{d}p\\&=1-\int_{-\infty}^{+\infty}f_{P_1^{h_{\mathrm{T}}h_{\mathrm{R}}}}(p)\,\mathrm{d}p\\&\quad+\int_{\mathcal{N}\upsilon}^{+\infty}F^{n-1}_{P_{l\geq 2}^{h_{\mathrm{T}}h_{\mathrm{R}}}}\left(\frac{p}{\upsilon}-\mathcal{N}\right)f_{P_1^{h_{\mathrm{T}}h_{\mathrm{R}}}}(p)\,\mathrm{d}p,\end{aligned} \tag{65}$$

which, being the first integral in the last step equal to one, finally provides the second case in (33).

G. Proof of Lemma 5

Apply the mean of a function of a discrete rv by using (2) and (4). This yields [24]:

$$\begin{aligned}\mathcal{E}_\epsilon(\bar{b})&=1-\mathbb{E}_B[\mathcal{O}_\epsilon(B)]=1-\sum_{n=1}^{+\infty}\mathcal{O}_\epsilon(b)f_B(b;\bar{b})\\&=1-\epsilon\frac{\tau_{\mathrm{H}}}{\tau(\bar{b}-1)}\sum_{n=1}^{+\infty}\frac{1}{b}\left(1-\frac{1}{\bar{b}}\right)^b,\end{aligned} \tag{66}$$

from which, by remembering the Maclaurin series for the natural logarithm, one immediately obtains (34).

H. Proof of Proposition 3

Use (1) in (37), apply the binomial row-symmetry property, and remember (39), thus obtaining:

$$\begin{aligned}T^1_{\mathbf{s}'\mathbf{s}}(\varsigma,\upsilon)&=\xi^1_{\mathbf{s}'\mathbf{s}}(\varsigma)\sum_{k=\tilde{k}_{\mathrm{i}}}^{\tilde{k}_{\mathrm{e}}}\binom{d'}{d-k}\left[\eta^1_{\mathbf{s}'}(\upsilon)\right]^k\\&\left\{\sum_{k'=\tilde{k}'_{\mathrm{i}}}^{\tilde{k}'_{\mathrm{e}}}\binom{i'}{k+k'}\binom{k+k'}{k}\binom{o'}{o-k'}\left[1-\eta^1_{\mathbf{s}'}(\upsilon)\right]^{k'}\right\},\end{aligned} \tag{67}$$

from which, by applying the subset-of-a-subset property to the first two binomials of the second summation, one derives (38).

I. Proof of Proposition 4

Similarly to *Proposition 3*, use (1) in (45) and apply the binomial row-symmetry property, hence obtaining:

$$\begin{aligned}T^2_{\mathbf{s}'\mathbf{s}}(\varsigma,\upsilon)&=f_I(i;\varsigma)\frac{(\bar{b}-1)^d}{\bar{b}^{i'+d'}}\sum_{k=\hat{k}_{\mathrm{i}}}^{\hat{k}_{\mathrm{e}}}\binom{d'}{d-k}\left[\eta^2_{\mathbf{s}'}(\upsilon)\right]^k\\&\left\{\sum_{k'=0}^{i'-k}\binom{i'}{k+k'}\binom{k+k'}{k}(\bar{b}-1)^{k'}\left[1-\eta^2_{\mathbf{s}'}(\upsilon)\right]^{k'}\right\}\\&=f_I(i;\varsigma)\frac{(\bar{b}-1)^d}{\bar{b}^{i'+d'}}\sum_{k=\hat{k}_{\mathrm{i}}}^{\hat{k}_{\mathrm{e}}}\binom{i'}{k}\binom{d'}{d-k}\left[\eta^2_{\mathbf{s}'}(\upsilon)\right]^k\\&\quad\left\{1+(\bar{b}-1)\left[1-\eta^2_{\mathbf{s}'}(\upsilon)\right]\right\}^{i'-k},\end{aligned} \tag{68}$$

where the summation on the index k' is solved by employing the subset-of-a-subset property and then the binomial theorem. Few algebra and the use of (47) finally lead to (47).

REFERENCES

[1] L. U. Khan, W. Saad, D. Niyato, Z. Han, and C. S. Hong, "Digital-twin-enabled 6G: Vision, architectural trends, and future directions," *IEEE Commun. Mag.*, vol. 60, no. 1, pp. 74–80, Jan. 2022.

[2] F. Shan, H. Huo, J. Zeng, Z. Li, W. Wu, and J. Luo, "Ultra-wideband swarm ranging protocol for dynamic and dense networks," *IEEE/ACM Trans. Netw.*, vol. 30, no. 6, pp. 2834–2848, Dec. 2022.

[3] D. Palossi et al., "Fully onboard AI-powered human-drone pose estimation on ultralow-power autonomous flying nano-UAVs," *IEEE Internet Things J.*, vol. 9, no. 3, pp. 1913–1929, Feb. 2022.

[4] F. Y. Hadaegh, S.-J. Chung, and H. M. Manohara, "On development of 100-gram-class spacecraft for swarm applications," *IEEE Syst. J.*, vol. 10, no. 2, pp. 673–684, Jun. 2016.

[5] M. Vaezi et al., "Cellular, wide-area, and non-terrestrial IoT: A survey on 5G advances and the road towards 6G," *IEEE Commun. Surv. Tut.*, vol. 24, no. 2, pp. 1117–1174, Secondquarter 2022.

[6] J. Iannacci, "A perspective vision of micro/nano systems and technologies as enablers of 6G, super-IoT, and tactile internet," *Proc. IEEE*, vol. 111, no. 1, pp. 5–18, Jan. 2023.

[7] R. R. Choudhury, X. Yang, R. Ramanathan, and N. H. Vaidya, "On designing MAC protocols for wireless networks using directional antennas," *IEEE Trans. Mobile Comput.*, vol. 5, no. 5, pp. 477–491, May 2006.

[8] H. Singh and S. Singh, "DOA-ALOHA: Slotted ALOHA for ad hoc networking using smart antennas," in *Proc. IEEE Veh. Technol. Conf.*, 2003, pp. 2804–2808.

[9] T. Korakis, G. Jakllari, and L. Tassiulas, "CDR-MAC: A protocol for full exploitation of directional antennas in ad hoc wireless networks," *IEEE Trans. Mobile Comput.*, vol. 7, no. 2, pp. 145–155, Feb. 2008.

[10] J.-J. Chang, W. Liao, and J.-R. Lai, "On reservation-based MAC protocol for IEEE 802.11 wireless ad hoc networks with directional antenna," *IEEE Trans. Veh. Technol.*, vol. 60, no. 6, pp. 2669–2679, Jul. 2011.
[11] F. Babich, M. Comisso, A. Crismani, and A. Dorni, "On the design of MAC protocols for multi-packet communication in IEEE 802.11 heterogeneous networks using adaptive antenna arrays," *IEEE Trans. Mobile Comput.*, vol. 14, no. 11, pp. 2332–2348, Nov. 2015.
[12] P.-C. Yeh, W. E. Stark, and S. A. Zummo, "Performance analysis of wireless networks with directional antennas," *IEEE Trans. Veh. Technol.*, vol. 57, no. 5, pp. 3187–3199, Sep. 2008.
[13] H. Ju, D. Kim, H. V. Poor, and D. Hong, "Bi-directional beamforming and its capacity scaling in pairwise two-way communications," *IEEE Trans. Wireless Commun.*, vol. 11, no. 1, pp. 346–357, Jan. 2012.
[14] S. Singh, R. Mudumbai, and U. Madhow, "Interference analysis for highly directional 60-GHz mesh networks: The case for rethinking medium access control," *IEEE/ACM Trans. Netw.*, vol. 19, no. 5, pp. 1513–1527, Oct. 2011.
[15] H. Shokri-Ghadikolaei and C. Fischione, "The transitional behavior of interference in millimeter wave networks and its impact on medium access control," *IEEE Trans. Commun.*, vol. 64, no. 2, pp. 723–740, Feb. 2016.
[16] A. Thornburg, T. Bai, and R. W. Heath Jr., "Performance analysis of outdoor mmWave ad hoc networks," *IEEE Trans. Signal Process.*, vol. 64, no. 15, pp. 4065–4079, Aug. 2016.
[17] X. Yu, J. Zhang, M. Haenggi, and K. B. Letaief, "Coverage analysis for millimeter wave networks: The impact of directional antenna arrays," *IEEE J. Sel. Areas Commun.*, vol. 35, no. 7, pp. 1498–1512, Jul. 2017.
[18] M. Comisso and F. Babich, "Coverage analysis for 2D/3D millimeter wave peer-to-peer networks," *IEEE Trans. Wireless Commun.*, vol. 18, no. 7, pp. 3613–3627, Jul. 2019.
[19] S. J. Maeng, M. A. Deshmukh, İ. Güvenç, A. Bhuyan, and H. Dai, "Interference analysis and mitigation for aerial IoT considering 3D antenna patterns," *IEEE Trans. Veh. Technol.*, vol. 70, no. 1, pp. 490–503, Jan. 2021.
[20] F. Babich, F. Vatta, G. Buttazzoni, and M. Comisso, "Random directional access with and without feedback for 5G/6G peer-to-peer networks," in *Proc. IEEE Int. Conf. Commun.*, 2023, pp. 4822–4827.
[21] C. N. Barati et al., "Initial access in millimeter wave cellular systems," *IEEE Trans. Wireless Commun.*, vol. 15, no. 12, pp. 7926–7940, Dec. 2016.
[22] W. Attaoui, K. Bouraqia, and E. Sabir, "Initial access & beam alignment for mmWave and terahertz communications," *IEEE Access*, vol. 10, pp. 35363–35397, 2022.
[23] L. Kleinrock and F. A. Tobagi, "Packet switching in radio channels: Part I - Carrier sense multiple-access modes and their throughput-delay characteristics," *IEEE Trans. Commun.*, vol. 23, no. 12, pp. 1400–1416, Dec. 1975.
[24] R. D. Yates and D. J. Goodman, *Probability and Stochastic Processes*. New York, NY, USA: Wiley, 1999.
[25] J.-B. Seo, B. C. Jung, and H. Jin, "Nonorthogonal random access for 5G mobile communication systems," *IEEE Trans. Veh. Technol.*, vol. 67, no. 8, pp. 7867–7871, Aug. 2018.
[26] E. Casini, R. D. Gaudenzi, and O. d. R. Herrero, "Contention resolution diversity slotted ALOHA (CRDSA): An enhanced random access scheme for satellite access packet networks," *IEEE Trans. Wireless Commun.*, vol. 6, no. 4, pp. 1408–1419, Apr. 2007.
[27] E. Paolini, G. Liva, and M. Chiani, "Coded slotted ALOHA: A graph-based method for uncoordinated multiple access," *IEEE Trans. Inf. Theory*, vol. 61, no. 12, pp. 6815–6832, Dec. 2015.
[28] M. D. Renzo, "Stochastic geometry modeling and analysis of multi-tier millimeter wave cellular networks," *IEEE Trans. Wireless Commun.*, vol. 14, no. 9, pp. 5038–5057, Sep. 2015.
[29] M. R. Akdeniz et al., "Millimeter wave channel modeling and cellular capacity evaluation," *IEEE J. Sel. Areas Commun.*, vol. 32, no. 6, pp. 1164–1179, Jun. 2014.
[30] P. K. Sharma and D. I. Kim, "Random 3D mobile UAV networks: Mobility modeling and coverage probability," *IEEE Trans. Wireless Commun.*, vol. 18, no. 5, pp. 2527–2538, May 2019.
[31] F. D. Nunes and F. M. G. Sousa, "Generalized gamma fading simulation of scintillation disturbed GNSS signals," *IEEE Trans. Aerosp. Electron. Syst.*, vol. 54, no. 4, pp. 2025–2034, Aug. 2018.
[32] J. F. Hayes and T. V. J. G. Babu, *Modeling and Analysis of Telecommunications Networks*. New York, NY, USA: Wiley, 2004.
[33] H. T. Chattha, M. K. Ishfaq, B. A. Khawaja, A. Sharif, and N. Sheriff, "Compact multiport MIMO antenna system for 5G IoT and cellular handheld applications," *IEEE Antennas Wireless Propag. Lett.*, vol. 20, no. 11, pp. 2136–2140, Nov. 2021.

Massimiliano Comisso (Member, IEEE) received the M.Sc. degree in electronic engineering and the Ph.D. degree in information engineering from the University of Trieste, Trieste, Italy, in 2003 and 2007, respectively. He was with Alcatel on DWDM systems and collaborated with Danieli Automation on electromagnetic NDE models. He is currently an Associate Professor in communication networks and waveguide/optical systems with the Department of Engineering and Architecture (DIA), University of Trieste. He is author/coauthor of more than 100 international scientific papers and is Referee/TPC Member for several IEEE journals and conferences. He has been Best Student Paper Award (BPA) finalist at IEEE GLOBECOM'06 and was the recipient of the BPA at IEEE CAMAD'09. His research interests include distributed wireless networks, millimeter-wave communications, antenna array synthesis, and small antennas.

Francesca Vatta (Member, IEEE) received the M.Sc. degree in electronic engineering and the Ph.D. degree in telecommunications from the University of Trieste, Trieste, Italy, in 1992 and 1998, respectively. She was with the Department of Engineering and Architecture (DIA), University of Trieste in 1999, where she is currently an Assistant Professor of information theory and error-control coding. Starting in 2002 and 2005, she has been visiting scholar, respectively, at Notre Dame University, Dame, IN, USA, cooperating with the Coding Theory Research Group (RG) under the guidance of Prof. D.J. Costello, Jr., and Ulm University, Ulm, Germany, cooperating with the Telecommunications and Applied Information Theory RG under the guidance of Prof. M. Bossert. She is author/coauthor of more than 100 papers published on international journals and conference proceedings. Her research interests include the area of channel coding concerning, in particular, the analysis and design of capacity achieving codes.

Giulia Buttazzoni (Member, IEEE) received the M.Sc. degree (*summa cum laude*) in telecommunication engineering and the Ph.D. degree in information engineering from the University of Trieste, Trieste, Italy, in 2008 and 2013, respectively. In 2014, she was with the Department of Engineering and Architecture (DIA), University of Trieste, where she is currently Associate Professor in electromagnetic fields and antennas. She is Member of SIEM (Italian Electromagnetics Society) and CNIT (National Inter-University Consortium for Telecommunications). Her research interests include antenna array synthesis techniques and numerical methods for electromagnetic fields.

Fulvio Babich (Senior Member, IEEE) received the M.Sc. degree (*summa cum laude*) in electrical engineering, University of Trieste, Trieste, Italy, in 1984. After graduation he was with Research and Development Laboratories, Telettra, Benevento, Italy, where he was engaged in optical fiber communications. He was with Zeltron as a Communication System Engineer, responsible of the activities within the ESPRIT program. In 1992, He was with the Department of Engineering and Architecture (DIA), University of Trieste, where he is Full Professor of Digital Communications and Wireless Networks. She is a Member of the Board of GTTI (National Telecommunications and Information Theory Group) and Directive Board of CNIT (National Inter-University Consortium for Telecommunications) and Coordinator of the Ph.D. Board in Industrial and Information Engineering of the University of Trieste. His research interests include the field of wireless networks and millimeter wave communications. He is involved in channel modeling, multiple access techniques, channel coding, error control techniques, and cross-layer design.